Porous plasticity revisited: Macroscopic and multiscale modeling

Gilles Rousselier

Version of Record: https://www.sciencedirect.com/science/article/pii/S0749641920304861
Manuscript_0a6c0e3649e51ee16e0479b0135725a8

Porous plasticity revisited: macroscopic and multiscale modeling.

Gilles Rousselier[1*]

[1]*MINES ParisTech, PSL University, MAT-Centre des Matériaux, CNRS UMR 7633,*

BP 87, 91003 Evry Cedex, France

Abstract

Porous plasticity aims to model the growth and coalescence of voids leading to ductile failure. The GTN model (1984), resulting from heuristic modifications to Gurson's homogenized hollow sphere model (1977), is used in numerous publications. The Rousselier model (1981), developed in the framework of continuum thermodynamics, is apparently similar. Both models are effective in numerical calculations, but the reasons why they perform well were not investigated in details in the existing literature, as regards transition to uniaxial deformation, relations between various modes of strain localization, finite element discretization, regularization. In the present paper, we propose first to revisit both models and to compare their fundamentally different mechanical behaviors. For stress triaxiality *larger* than some critical value, it is shown that theoretically the GTN model cannot achieve strain localization *in a plane* but only *pointwise* localization for the ultimate mechanical state (stress tensor equal to zero). The larger the void volume fraction (void growth), the smaller the stress triaxiality critical value. Fortunately, discretization transforms the pointwise localization into *volume* localization and with an appropriate Cartesian finite element mesh a more or less planar sheet of integration points can be obtained. The Rousselier model can achieve strain localization in a plane at all stress triaxialities and discretization also transforms this localization into volume localization with a characteristic element size. Second, multiscale modeling of *both* plasticity and ductile damage (*not* limited to void damage) is an essential way of progress for laboratory specimen calculations. The Rousselier model can be incorporated into polycrystalline models based on crystal plasticity, with reasonable computation times provided a *reduced texture* with a small number of crystallographic orientations is used. It can be coupled with a new Coulomb ductile fracture model at the slip system scale and with secondary void

nucleation and growth models at the grain and slip system scales, respectively. The multiscale model is applied to aluminum CT and KAHN specimens and to steel round notched specimens.

Keywords: Micromechanics; Continuum Thermodynamics; Strain Localization; Void Coalescence; Secondary Void Nucleation.

* Corresponding author. Tel.: 33 1 60 76 30 21; fax: 33 1 60 76 31 50
E-mail address: gilles.rousselier@mines-paristech.fr (G. Rousselier)

Highlights:

1. Although apparently similar, the Gurson and Rousselier plastic potentials have different mechanical consequences.
2. For both models, finite element discretization yields *volume* localization only, leading to strain localization in a plane.
3. The Rousselier model can be incorporated into *homogenized polycrystalline* models.
4. It can be coupled with other plasticity and ductile damage models at various scales.
5. Finite element *multiscale* modeling of aluminum and steel laboratory specimens enables predictions of slant fracture and secondary voids effects in both materials.

1. Introduction

Ductile failure can be defined in a very general way as a damage mechanism involving a gradual and significant dissipation of mechanical energy, at several scales. In metallic alloys, the most commonly observed (but not unique) ductile failure mechanism is nucleation, growth by plastic deformation and coalescence of microscopic voids. More than fifty years ago, micromechanical models of an isolated void in a matrix were developed by McClintock (1968) and Rice and Tracey (1969). An exponential dependence of void growth on stress triaxiality was obtained. Following Rice's work, Gurson (1977) published constitutive equations for a porous ductile solid based on homogenization theory. An approximate limit analysis of a rigid-plastic hollow sphere with axisymmetric boundary conditions yields a plastic potential depending on the first and second invariants of the stress tensor and on the void volume fraction. It shows a quadratic dependence on von Mises equivalent stress and a hyperbolic cosine dependence on stress

triaxility $\eta = \sigma m/\sigma flow$ ($\sigma flow$ is a constant material parameter). The flow rules for both deviatoric and volumetric plastic strain rates are obtained by derivation of the plastic potential (normality rule). Later, another porous plasticity model was developed by Rousselier (1981) in the framework of continuum thermodynamics with the hypothesis of two scalar internal variables for plasticity and damage, respectively. Continuum thermodynamics is a powerful concept for the construction of models that are as simple as possible (Germain et al., 1983). The exponential dependence of void growth on stress triaxiality is derived from the *generalized* normality rule, i.e. normality for both plastic strain rate and internal variables rates.

In the numerical analysis of a doubly periodic array of cylindrical voids, Tvergaard (1981) obtained *shear band* instabilities at critical strains that are twice smaller than the ones predicted by the Gurson model. It is the origin of Gurson's model second *heuristic* modification (the first one is the substitution of the constant $\sigma flow$ by a hardening flow stress σM). With three additional parameters q_1, q_2 and q_3, Tvergaard could not fit all the numerical predictions simultaneously, but a considerable improvement was found with $q1 = 1.5$, $q2 = 1$ and $q3 = (q1)^2$. These values are very rarely revisited in the numerous publications based on Gurson's model: see the summary tables in Benseddiq and Imad (2008), Yildiz and Yilmaz (2020), although the model is generally applied to configurations that are not shear-dominated.

Actually in these configurations stress triaxiality is large (say $\eta = \sigma_m / \sigma_{eq} > 1$, ratio of hydrostatic stress to von Mises equivalent stress) and failure by void coalescence takes place in a plane normal to the main loading direction (at the macroscopic scale, even if a zig-zag crack may be observed at a smaller scale), corresponding to void coalescence models like Thomason's (1985). Gurson's model is based on the assumption that void growth is driven by some diffuse plastic flow in the matrix. Therefore this model is not expected to model the flow localization that takes place between voids. That is why Tvergaard and Needleman (1984) introduced a third heuristic modification to account for void coalescence, supposed to occur at a critical void volume fraction $f = fc$. The void growth rate is then *discontinuously* accelerated by a large factor K (say $K = 3$ or even larger), which triggers void coalescence. The accelerated void volume fraction f^* replaces f in the equations but the latter still is the "physical" value to be compared with experimental data, because the *ultimate* value $f^*_U = 1/q1$ (if $q3 = q1^2$) at which the stress carrying capacity vanishes is unrealistically large. The experimental porosity at complete failure

is typically 0.2 or less, the one predicted using micromechnical studies ranges between 0.15 and 0.30 (Benzerga and Leblond, 2010). With these various heuristic modifications of the Gurson model, the so-called GTN model enabled the finite element modeling of cup-cone fracture in a round tensile bar. In contrast, the Rousselier model without any modification enabled the finite element modeling of crack initiation and propagation in a single edge cracked flat tension specimen (Rousselier, 1981). In the last forty years, the research field of porous materials has been continuously investigated, e.g. recently: Monchiet et al. (2008), Besson (2009), Seidenfuß et al. (2011), Guo et al. (2013), Tu et al. (2013), Malcher et al. (2014), Vincent et al. (2014), Ling et al. (2016), Leclerc et al. (2020), Chen et al. (2020), Fehringer and Seidenfuß (2020).

An important advantage of the Rice-Gurson method is that it can provide numerous extended models. They are detailed in a recent review paper (Benzerga et al., 2016), e.g. the Gologanu-Leblond-Devaux model for spheroidal voids, the Madou-Leblond model for ellipsoidal voids, models incorporating plastic anisotropy with a Hill matrix (Benzerga and Besson, 2001), etc. Another extension is the consideration of micro-inertia effects in the vicinity of collapsing voids (Sartori et al., 2015; Wilkerson, 2017; Czarnota et al., 2020). The derivation of a simple model with continuum thermodynamics only succeeds in the case of isotropic damage and the Rousselier model cannot be extended easily. Nevertheless, this model can be incorporated into *polycrystalline* models based on crystal plasticity (Rousselier and Leclercq, 2006). The analytical form of Gurson's model makes it impossible to incorporate into self-consistent *polycrystalline* plasticity with a homogenized flow equation. It is a limitation if we consider that multiscale modeling of *both* plasticity and ductile damage (*not* limited to void damage) is an essential way of progress for laboratory specimen calculations, with reasonable computation times because of reduced texture identification (8 to 15 crystal orientations), e.g. Luo and Rousselier (2014), Rousselier and Luo (2014), Rousselier and Quilici (2015), Rousselier et al. (2017). It enables a better modeling of kinematic, anisotropic and latent hardening and also the coupling with other plasticity and ductile damage models at various scales. The multiscale model is applied here to aluminum CT and KAHN specimens and to steel round notched specimens.

The paper is organized as follows. The constitutive equations of the GTN and Rousselier models are recalled in Section 2. The ability of the porous plasticity constitutive equations to localize plastic flow *in a plan*e is a crucial feature for ductile fracture modeling. It has not been investigated from a practical point of view in existing literature. In Section 3, the necessary

kinematic condition of *planar* macroscopic localization (NKCPML) and its consequences for both models are presented. The evolution of the yield surfaces with increasing void volume fraction and localization in a finite element mesh are investigated. A general discussion of the macroscopic porous plasticity models concludes this Section. Section 4 is devoted to multiscale modeling: integration of porous plasticity into homogenized polycrystalline models, examples of numerical simulations of laboratory specimens.

2. Macroscopic porous plasticity constitutive equations.

After the earlier work of McClintock (1968), the founding model is the one of Rice and Tracey (1969) which gives the growth rate of an isolated spherical void of radius R (transposable to the volume fraction f) as a function of stress triaxiality η:

$$\dot{f}/f = 3\dot{R}/R = \dot{p}D_1 \exp(Q\eta), \qquad \eta = \sigma_m/\sigma_p\ , \qquad \dot{p} = \dot{\varepsilon}^p_{eq} \quad \text{(von Mises)} \tag{1}$$

where σ_m is the mean hydrostatic stress and σ_p is the plastic flow stress, a constant in the original model. Rice and Tracey decomposed the velocity field into volume-changing and shape-changing parts. They assumed that the shape-changing part does not contribute to the void growth at high stress triaxiality. The theoretical values of the constant parameters are Q = 1.5 and D_1 = 0.850. Usually, the exponent is written as $3\sigma m/2\sigma p$, the exact factor Q = 3/2 being given by the high stress triaxiality case, equation (37) in Rice and Tracey's paper. The exponential dependence is in agreement with early void growth measurements (e.g. Marini et al., 1985; Rousselier, 1987) and confirmed with X-ray microtomography (e.g. Maire et a1., 2011; Landron et al., 2011), with Q = 1.5 but however a larger experimental value D_1 = 1.1 to 3.6 depending on the metallic alloy. Assuming that the shape-changing part has an effect on void growth, Huang (1991) obtained a corrected value D_1 = 1.275 for the second parameter, closer to the experimental results but still too small for many alloys. With an adequate value for the parameter D_1, Rice and Tracey's model is a strong basis.

The Gurson model (Gurson, 1977; Tvergaard, 1981) is a plastic flow surface obtained by homogenization of a hollow sphere with two kinematic fields (volume-changing and shape-changing displacement rates).

$$\sigma_{eq}^2/\sigma_p^2-(1+q_3f^2)+2q_1f\cosh(Qq_2\eta)=0,\quad 3\dot{\varepsilon}_m^p=\dot{f}/(1-f)=2\dot{p}D_1f\sinh(Qq_2\eta) \tag{2}$$

In the original model, $q1 = q2 = q3 = 1$. The flow stress $\sigma_p(p)$ takes into account work hardening in the GTN model (Tvergaard and Needleman, 1984). The second equation (2_2) is given by the mass conservation law and the normality rule. The parameters are $Q = 3/2$ and $D_1 = 3q1q2/4$. With the values recommended by Tvergaard (1981): $q1$=1.5, $q2$=1, $q3$=$q1^2$, we obtain $D_1 = 1.125$, which remains too small compared to experimental data (all the more with sinh < exp/2).

The void growth acceleration function is (Tvergaard and Needleman, 1984):

$$f^* = f \text{ for } f \le f_C,\ f^*(f) = f_C + K(f - f_C) \text{ for } f > f_C,\ K=\frac{f^*_U - f_C}{f_F - f_C},\ f^*(f_F) = f^*_U \tag{3}$$

The ultimate value at which the stress carrying capacity vanishes is $f^*_U=(q_1-\sqrt{q_1^2-q_3})/q_3$. This ultimate state cannot be obtained for $q3 > q1^2$. For $q3 \le q1^2$, f^*_U decreases very rapidly from the maximum value $f^*_{Umax} = 1/q1$ for $q3 = q1^2$, where the slope is infinite (Fig. 1). For $q3 = 1$, f^*_U is not so unrealistically large than f^*_{Umax} (e.g. $f^*_U = 0.382$ for $q1 = 1.5$ instead of $1/q1 = 0.667$). Nevertheless, $q3 = 1$ was never used according to the existing literature (Yildiz and Yilmaz, 2020).

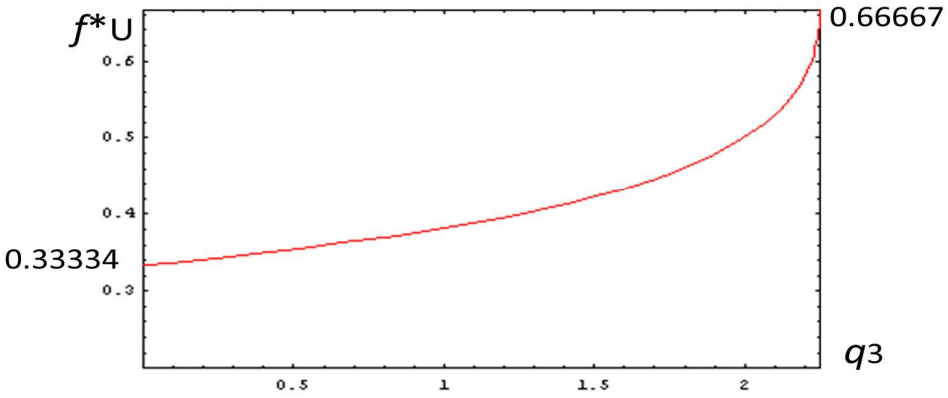

Figure 1. Ultimate value f^*_U in function of $q3$ for a given $q1$ (here $q1 = 1.5$, range $q3 = 0$ - 2.25).

Like Gurson's, the Rousselier plastic potential (Rousselier, 1981, 1987, 1989; Germain et al., 1983) is the sum of 3 terms, but the analytical form, deduced from continuum thermodynamics and from the *generalized* normality rule, is different :

$$\frac{\sigma_{eq}}{1-f} - H(p,\dot{p},T) + \sigma_1 D_1 f \exp\left(\frac{\sigma_m}{(1-f)\sigma_1}\right) = 0\,, \qquad 3\dot{\varepsilon}^p_m = \dot{p} D_1 f \exp\left(\frac{\sigma_m}{(1-f)\sigma_1}\right) \tag{4}$$

Continuum thermodynamics is only used to obtain the analytical form of the porous plastic potential. It is out of the scope of the present paper to discuss the convexity and its consequences for dissipation and numerical implementation (Enakoutsa et al., 2007). This framework is effective in the simplest case of isotropic damage, i.e. the porosity is characterized by its volume fraction f only. (In Rousselier (1981, 1987, 1989), the internal variable β is used in place of f but it does not impact the model because a functional relation exists between f and β.) The detailed micromechanisms are not considered explicitly (the multiscale framework is better suited to model these mechanisms, see Section 4). The detailed derivation of the model is given in Appendix B of Rousselier and Luo (2014).

The three phases of void damage are void nucleation, growth and coalescence. Specific models are used for void nucleation (e.g. Chu and Needleman, 1980). In this Section, we only consider some initial value f_0 of the void volume fraction f . The scientific objective of porous plasticity is to model void growth and void coalescence. In the continuum thermodynamics framework, the Kirchhof stress $\underline{\tau} = \underline{\sigma}/\rho$ has to be used in place of the Cauchy stress $\underline{\sigma}$, with $\rho \cong (1-f)/(1-f_0)$. Assuming $f_0 << 1$, only $\underline{\sigma}/(1-f)$ remains. This point is important for the coalescence stage at large void volume fraction.

The viscoplastic flow stress is $\sigma_{vp} = H(p,\dot{p},T)$, depending on strain rate $\dot{p}$ and on temperature *T.* As in Rice and Tracey's and Gurson's original models and unlike the GTN model, the denominator in the exponential is a constant material parameter σ_1. Thermodynamics does not give the integration constants D_1 and σ_1. Generally, D_1=2 was used in applications (e.g. Lorentz et al., 2008; Seidenfuss et al., 2011; Tu et al., 2013). By analogy with Rice and Tracey's model, $Q\sigma_1 = (3/2)\sigma_1 = H(p_1,\dot{p},T)$ is assumed, at saturated strain hardening (Voce) for a large parameter $p = p_1$. If strain hardening does not saturate (Swift), σ_1 (or p_1) is a parameter to be

calibrated (Rousselier et al., 1989; Rousselier, 2001a). σ_1 parametrically depends on strain rate and on temperature, which enabled to model the ductility curve in the range $\dot{p} = 10^{-3}$-10^{+6} s^{-1}, including the "adiabatic nose" at very large strain rates because of inertia at the macroscopic scale (Rousselier, 2001b), not to be confused with inertia at the micro-scale mentioned in the introduction.

3. Consequences of the necessary kinematic condition of planar macroscopic localization (NKCPML).

3.1. NKCPML.

We consider the necessary condition for the final stage of void damage induced ductile fracture, first in the particular case of a band perpendicular to the larger principal strain rate direction. This case corresponds for example to the center of axisymmetric tensile specimens or to thick cracked specimens in mode I, with stress triaxiality at fracture initiation larger than 1. In Fig. 2a, the schematic material element expanding in direction 1 contains a band B in the final coalescence stage of ductile fracture. Because of large plastic softening in the band, the two right and left blocks A are in elastic unloading: their deformation rate is very small. Consequently, the band expands in direction 1 only: $\dot{\varepsilon}^p_{22} \cong \dot{\varepsilon}^p_{33} \cong 0$, $\dot{\varepsilon}^p_m \cong \dot{\varepsilon}^p_{11}/3$ and $\dot{\varepsilon}^p_{eq} \cong 2\dot{\varepsilon}^p_{11}/3$.

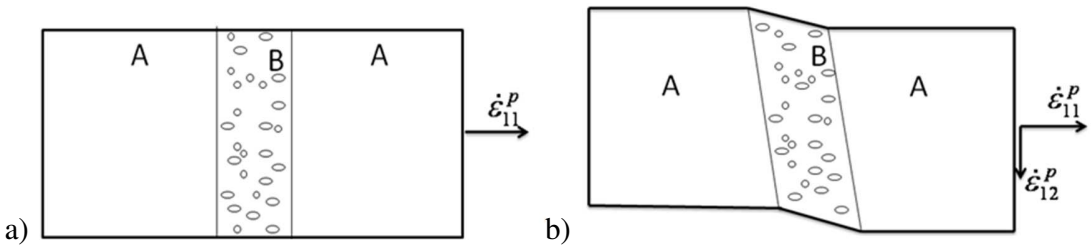

Figure 2. Material element containing two plastically inactive blocks A and a band B of strain and damage localization. The material element is expanding in direction 1. a) normal band without shear strain, b) slant band with shear strain.

The configurations of Fig. 2 are the same as in Rice (1976), but with negligible elastic strain rates. In the case of a localization plane perpendicular to the loading direction, Thomason (1985) was the first to mention that, at strain localization, uniaxial tension prevails and the lateral plastic strain rates are close to zero. In finite element calculations of cells with a spherical void, Koplik and Needleman (1988) also noticed that the beginning of coalescence in a plane perpendicular to the main loading direction corresponds to the *transition to uniaxial deformation*.

Therefore, the necessary kinematic coalescence condition is:

$$\dot{\varepsilon}^{p}_{eq} / \dot{\varepsilon}^{p}_{m} \cong 2 \tag{5}$$

In the case of a rate-independent material, the time at which this condition is met is close to the loss of ellipticity of the equilibrium equations which coincides with the condition det(nLn) = 0 in Rice (1976). In the case of a rate-dependent material, loss of ellipticity does not occur and it can be replaced by the stability analysis of a perturbation. Rice's localization condition corresponds to homogeneous fields (or to an infinite configuration), hence it slightly underestimates localization in a finite geometry (Besson et al., 2003). The coalescence model of Thomason (1985) comply with the condition of Eq. (5) in the particular case of Fig. 2a. The volumetric strain cannot be small: in flat ductile fracture, some amount of void damage is necessary.

In Figure 2b, the general case of a slant band is shown. It can generate a shear strain rate $\dot{\varepsilon}^{p}_{12} \neq 0$ and/or $\dot{\varepsilon}^{p}_{13} \neq 0$. Note that Hadamard's (1903) compatibility conditions only require that $\dot{\varepsilon}^{p}_{33} = 0$. Due to the additional strain rate terms, the equivalent strain rate $\dot{\varepsilon}^{p}_{eq}$ is larger than for a perpendicular band. The general necessary condition is $\dot{\varepsilon}^{p}_{m} \leq \dot{\varepsilon}^{p}_{eq} / 2$. Unlike Eq. (5) for the case of a perpendicular band, it is a loose condition, but still a necessary one. In slant and shear fracture, volumetric strain and void damage are not necessary, so $\dot{\varepsilon}^{p}_{m} = 0$ is possible, but they are not excluded, depending on the material.

The consequences of this necessary kinematic condition of *planar* macroscopic localization (NKCPML) are important. The yield locus must have a zone complying with Eq. (5). The larger this zone, the better the coalescence capability of the model. The yield locus of the Gurson model is plotted in Fig. 3 for a fairly large value $f = 0.1$. On the black curve, at large stress triaxiality,

localization in a plane is impossible because $\dot{\varepsilon}_m^p$ cannot be larger than $\dot{\varepsilon}_{eq}^p / 2$. At smaller stress triaxiality, only a small part of the yield locus enables localization in a plane approximately perpendicular to the main loading direction. For a constant stress triaxiality, Eq. (5) is only obtained during a small transient in the history of the increasing void volume fraction f, as shown in Fig. 4. For larger values of f, the yield locus shrinks to a quasi-circular ellipse until the ultimate state in which $f = f_U = f_F = 0.44480$, $\sigma m = \sigma eq = 0$. No particular direction stands out. At large stress triaxiality, the localization in the ultimate state is not planar but *pointwise*. The accelerated void growth rate of the GTN model, the pink arrow in Fig. 3, does not change this behavior.

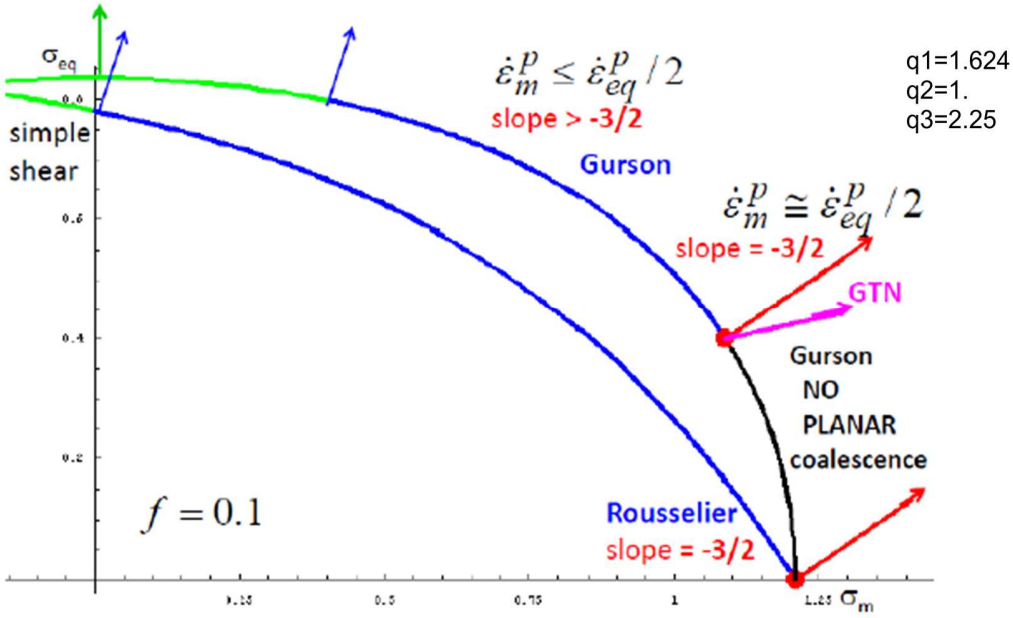

Figure 3. Gurson-GTN model yield locus in the (σ_m, σ_{eq}) plane for parameters: $f = 0.1$, Q=3/2, σp=1, $q_1 = 1.6245$, $q_2 = 1$, $q_3 = 2.25$. Rousselier porous plasticity model yield surface (blue curve) for parameters: $f_0 = 0$, $f = 0.1$, Q=3/2, $H = 1$, $\sigma 1 = H/Q = 2H/3$, $D_1 = 2$. NKCPML without and with shear strains, red arrows (slope -3/2) and blue arrows, respectively.

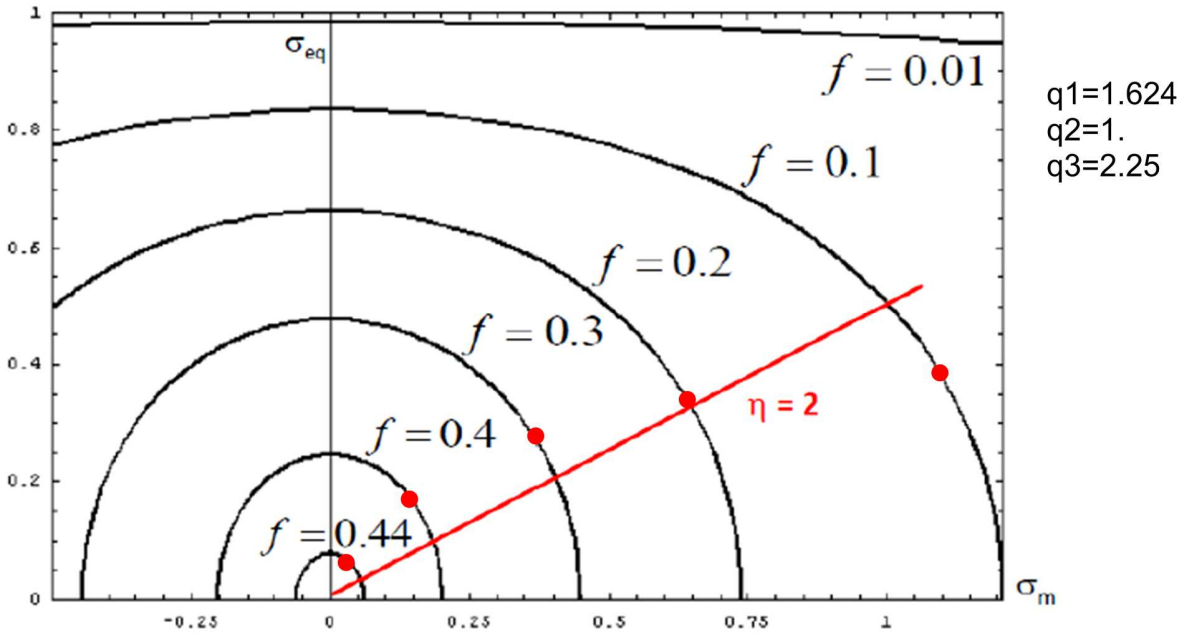

Figure 4. Gurson-GTN model, evolution of the yield locus in the (σ_m,σ_{eq}) plane with increasing void volume fraction for parameters: Q=3/2, σp=1, $q_1 = 1.6245$, $q_2 = 1$, $q_3 = 2.25$. The red line corresponds to a constant stress triaxiality equal to 2, the red discs correspond to the slope -3/2 (NKCPML).

With the Rousselier model in Figure 3, close to the vertex at $\tau_{eq} = \sigma_{eq} / \rho = 0$, the normality rule with Eq. (4) gives $\dot{\varepsilon}^p_{eq} / \dot{\varepsilon}^p_m \cong 3\sigma_1 / H$. With $Q = 3/2$ and $Q\sigma_1 = (3/2)\sigma_1 = H(p_1)$, the coalescence condition (5) is obtained *exactly* at the vertex. This is a remarkable consequence of the coefficient 3/2 in the exponent of Rice and Tacey's (1969) equation (37). Fig. 5 also shows that, for large void volume fraction, the yield locus is flat in the (σ_m,σ_{eq}) right quarter plane with a constant slope, i.e. that the coalescence condition (5) is obtained in a very large zone close to the vertex. At the opposite of the Gurson-GTN model, the larger the void volume fraction, the better achieved the condition of localization in a normal plane. In this region, the yield locus is quasi-identical to the one of Thomason's coalescence model, with the great difference that the orientation of the localization plane is predicted with the Rousselier model and not with Thomason's. If the latter was to be used as a plastic potential (Benzerga and Leblond, 2010), a number of yield loci with random orientations would have to be used, which considerably limits numerical applications.

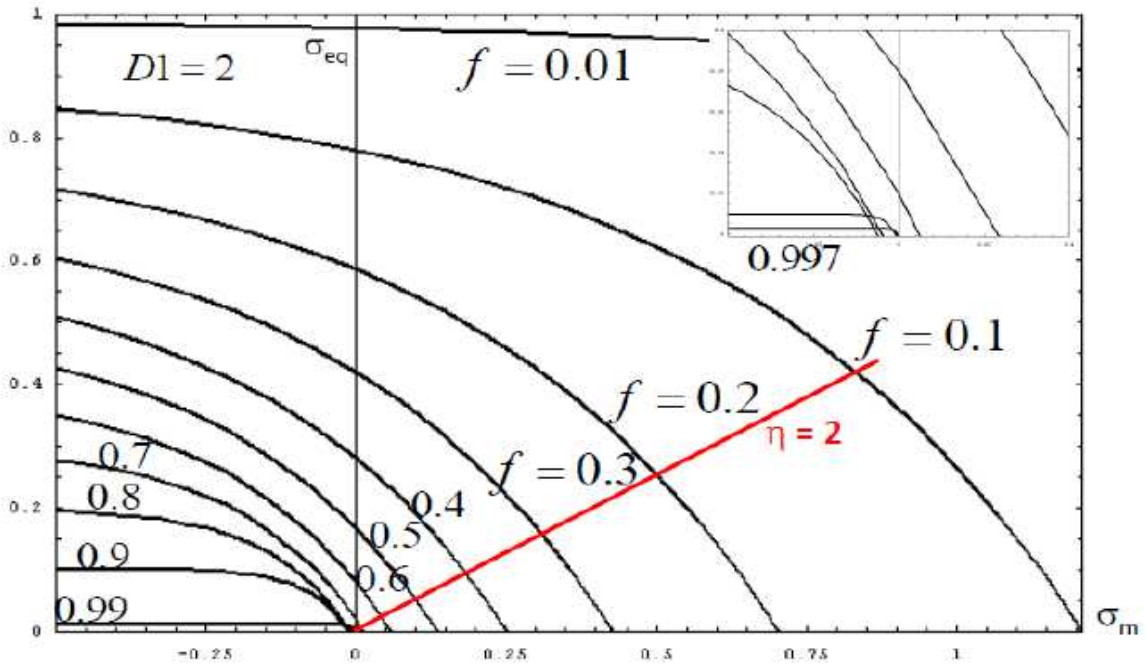

Figure 5. Rousselier model, evolution of the yield locus in the (σ_m, σ_{eq}) plane with increasing void volume fraction for parameters $f_0 = 0$, Q = 3/2, $H = 1$, $\sigma 1 = H/Q = 2H/3$, $D_1 = 2$. *Insert:* zoom close to the axes origin.

It can be noticed in the insert of Fig. 5 that for f larger than 0.75, approximately, σm is negative. Although ductile failure is obtained long before that value, this inconvenience can be avoided. Remarkably again, $\sigma m = 0$ for $f = 1$ is obtained *exactly* with $D1 = 3/2$, as shown in Figure 6. This value 3/2 is close to experimental data for many metallic alloys. The two constants $Q = 3/2$ and $D1 = 3/2$ are given by the mechanical analysis, but $D1 = 3/2$ is not mandatory.

In conclusion of this Subsection 3.1, it is highlighted that, despite apparently similar, the analytical forms of the Gurson-GTN and Rousselier models have fundamentally different mechanical consequences. These theoretical results are confronted with numerical applications in the next Subsection.

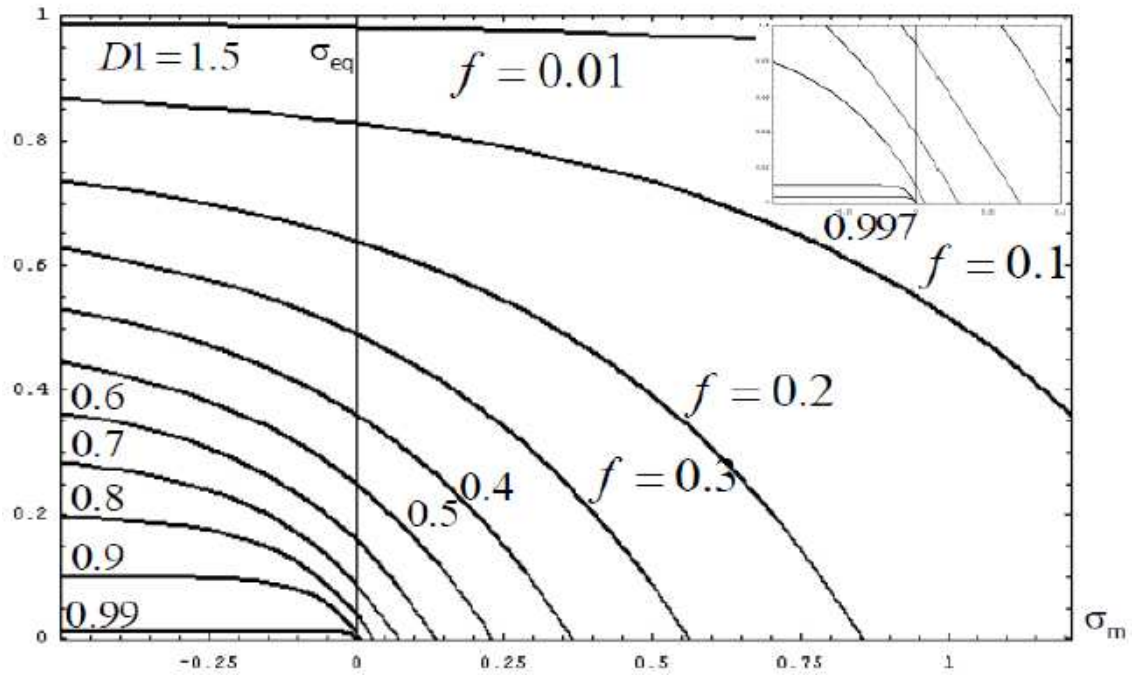

Figure 6. Rousselier model, evolution of the yield locus. Same as Fig. 5 with D_1 = 3/2 in place of $D_1 = 2$. *Insert:* zoom close to the axes origin.

3.2. Finite element modeling in porous plasticity.

The first finite element calculations in porous plasticity are the ones of Rousselier (1981) and Tvergaard and Needleman (1984). In the former, a pre-cracked three-point bent specimen is calculated in plane strain (2D). The mesh is made of quadrangles divided in two constant strain elements. In the crack plane, the quadrangle aspect ratio is 10/1 and the *height* of the elements is *lc* = 50 μm (Fig. 7). This large ratio is explained by the available rudimentary mesh tool and low computational capabilities. The results are mesh-size dependent and *lc* is the characteristic length (it is *not* the length of the elements as it is written in the figure). Fig. 7 shows strain localization, first in two elements at the crack tip and second along the straight crack path. Crack tip blunting is very poorly modeled by the coarse mesh.

The constants C = 1.5 and D = 0.49 = 0.283√3 mentioned in Fig. 7 correspond to Q = 3/2 and D_1 = D√3 = 0.85 of the original Rice and Tracey's publication (1969). The small value of D_1 is

compensated by the small value of $\sigma_1 = \sigma_0/Q$ with the initial yield stress $\sigma_0 = 500$ MPa compared to the saturated flow stress $2\sigma_0 = 1000$ MPa with the Voce hardening function $\sigma_0(2\text{-}\exp(-20p))$ used in the simulations.

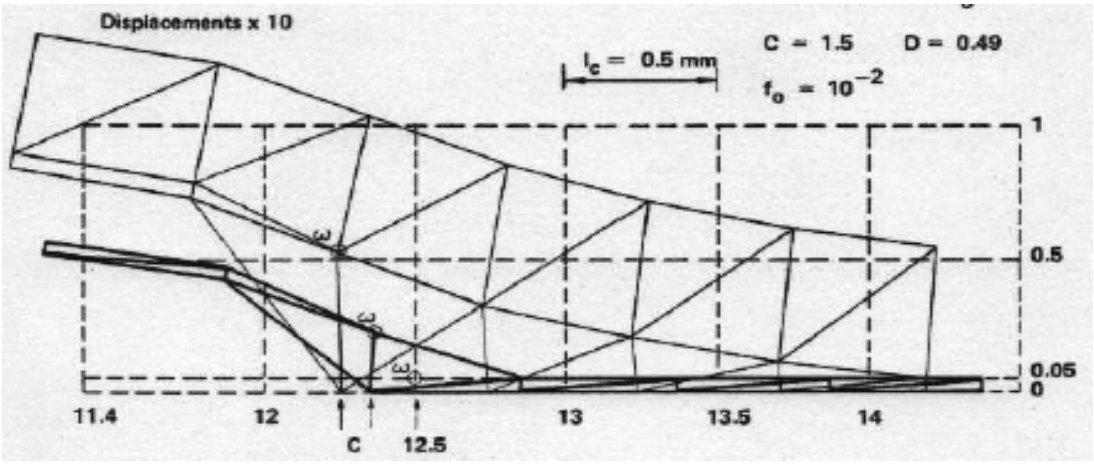

Figure 7. Pre-cracked three-point bent specimen (Rousselier, 1981), half mesh. Initial mesh (interrupted lines) and deformed meshes for two applied bending displacements showing strain localization in the initially thin elements. C (arrows) shows the crack tip.

In Fig. 8, the effect of the initial void volume fraction on the load-displacement curve is evidenced. After the beginning of strain localization, the local stress drops very rapidly (curves I and II). The corresponding finite elements can be considered as "broken" (small stress carrying capacity). In the 1981 paper, it is written and emphasized that: (i) "the ductile fracture properties of the metal are defined by two parameters: l_c, related to the interparticle spacing; and f_0, related to the particle volume fraction" and (ii) "stable crack growth occurs naturally, by localization of deformation, resulting from the constitutive relations only, without it being necessary to define a critical state nor to release the nodes as in usual models". These results were expected due to the possibility of strain localization in a plane with the constitutive model.

Conversely, the pointwise strain localization properties of the Gurson and GTN models could make it more difficult to obtain a plane crack. Consider the particular case of a round tensile

specimen, initially smooth or notched. In the center of the specimen, the axisymmetric triaxial stress field is the same as the remote field in Rice and Tracey (1969). Theoretically, pointwise localization will create a very small spherical volume with zero stress, that is to say a void. This is exactly the configuration of Rice and Tracey's model. Thus the void will grow with volume-changing and shape-changing parts and elongate in the tensile direction so as to become an axially symmetric ellipsoid. It will not become a plane crack.

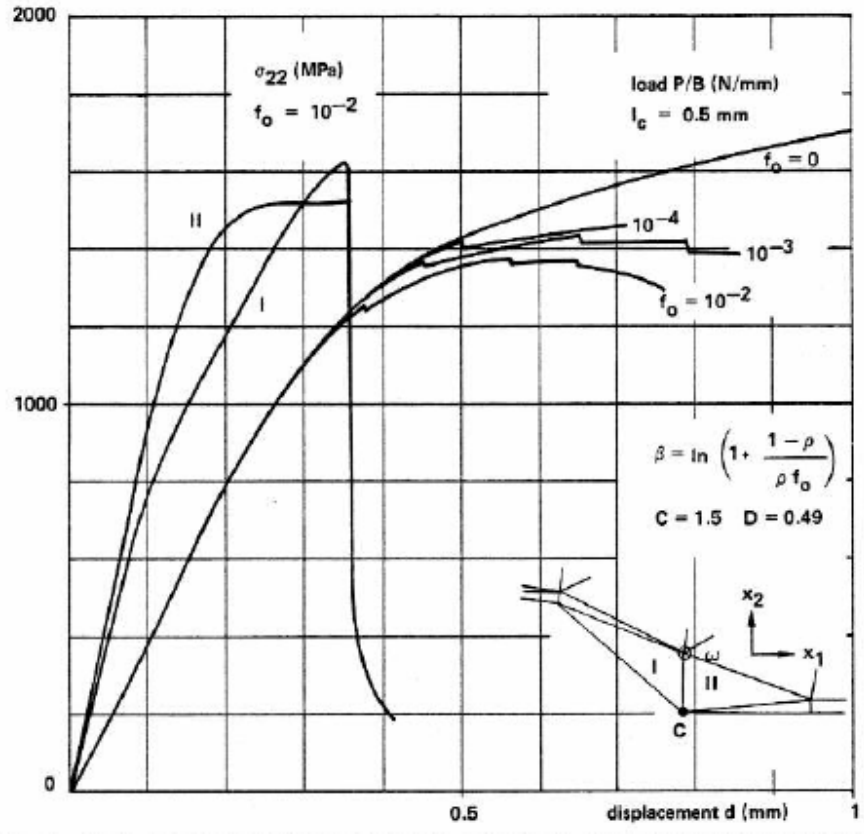

Figure 8. Pre-cracked three-point bent specimen (Rousselier, 1981). Load-displacement curves for initial void volume fraction f_0 = $10^{-2,}$ 10^{-3} and 10^{-4}. Stress component σ_{22} in the vertical direction for elements I and II at the crack tip. Note the functional expression of the damage variable β, with $\rho = (1-f)/(1-f_0)$.

However, in Tvergaard and Needleman (1984), a plane crack initiates and propagates in the center of a smooth tensile specimen (a small initial imperfection is introduced in the central section). This possible contradiction is not discussed in the 1984 paper, which is focused on the cup-cone transition. We have investigated the possible effect of finite element discretization. The axisymmetric mesh (2D) consists of quadrangles divided in four constant strain elements with a single central integration point in each triangle (Fig. 9, *right*). The initial aspect ratio is 10/1, the same as in Rousselier (1981).

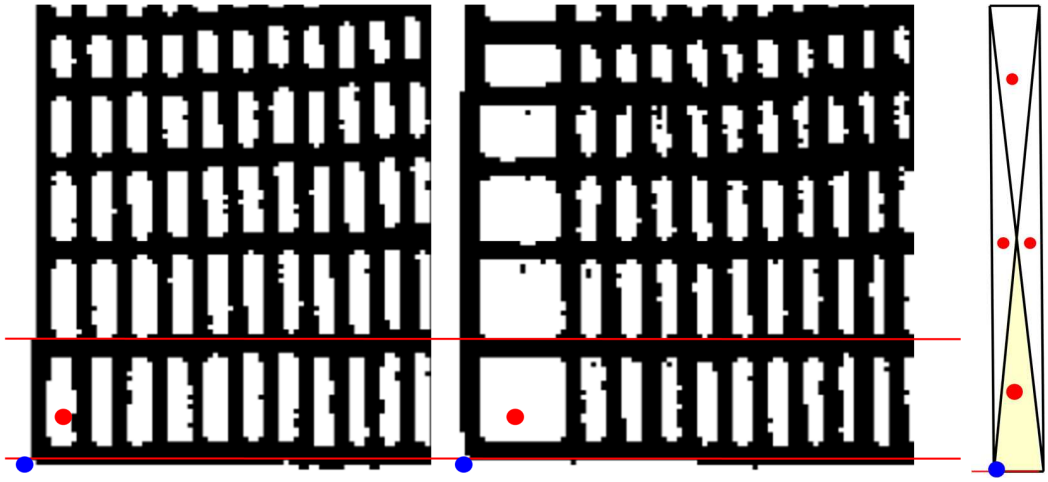

Figure 9. Central part of the smooth tensile specimen axisymmetric mesh (Tvergaard and Needleman, 1984). *Left*: deformed mesh immediately after the sharp "knee" of the load vs. axial strain curve, corresponding to $f = f_c = 0.15$ ($K = 5.2$). *Center:* Final deformed mesh. The blue disc is at the center of the specimen, the loading direction is horizontal. The red disc is the integration point closer to the center. *Right*: Initial geometry of the central quadrangle.

In Fig. 9, we have extracted the deformed meshes in the center of the specimen from the original figures of the paper. The two horizontal red lines demonstrate that the deformation is uniaxial at the beginning of strain localization, which is expected in a smooth tensile specimen close to the axis (left mesh) and also after complete strain localization (central mesh). The theoretical pointwise localization at the center of the specimen expected with the GTN model cannot be

observed because stress and strain are constant in each *finite* element (*finite* means with a volume that is not infinitesimal). Localization takes place first in the most deformed element (the larger red disc in Fig. 9, *right*) and *pointwise* localization (1D) is substituted with *finite volume* localization (3D). Next, localization will take place in a second finite element, etc. Because of the stress and strain fields in the central region of the tensile specimen, localization will propagate in a plane sheet of elements perpendicular to the main loading direction. From a *practical* point of view, the final result is not different from the one obtained with the Rousselier model because discretization transforms 1D (GTN) or 2D (Rousselier) localization into 3D localization. With quadratic finite elements, the result would be the same, each integration point being associated with some finite volume.

As already noted by Tvergaard and Needleman (1984), mesh design plays an important role in crack initiation and growth. It also affects the direction of crack propagation (Besson et al., 2001, 2003; Rousselier and Quilici, 2015). The problem lies in the softening models and in the resulting strain localization. In the case of the GTN model, the discontinuity of the derivative of the f^* function may inhibit slant fracture. A void nucleation model can be used to promote slant fracture but it is not satisfactory from a physical point of view (Benzerga and Leblond, 2010). Regularized models aim at suppressing this detrimental effect (Enakoutsa et al., 2007; Seidenfuss et al., 2011). It is not in the scope of the present paper to discuss the various regularization models. We just mention that regularization will have the same effect on the GTN model that finite element discretization: it will transform pointwise localization (1D) into volume localization (3D) and enable a more or less planar crack in a Cartesian finite element mesh. With the Rousselier model, the localization plane (2D) will get a defined thickness l_c (3D). For both models, the effect of mesh design is expected to be most reduced if not completely suppressed by regularization.

3.3. Discussion of the porous plasticity macroscopic models.

First, it can be stated that the investigation of void growth by plastic deformation with macroscale classical plasticity models only is an approximation. Grain size and void size are both at the microscale and the mechanisms of plastic deformation involved at this scale cannot be modeled with bulk material plasticity in the vicinity of a free surface. It is evidenced by the emerging slip bands observed at the inner *surface* of voids (Weck et al., 2008; Rousselier and

Quilici, 2015). The same kind of striations can be observed at the tip surface of a blunted initially sharp crack. Consequently, despite the simple approximate equation (2_2) that relates plastic strain and void growth rates, plasticity and void growth modeling *require* two *distinct* internal variables. These experimental observations also recall that theoretical and finite element analyses of unit cells, although very useful, are not to be confused with physical reality.

In Figure 10, a comparative summary of the GTN and Rousselier models characteristics is proposed. The first heuristic extension of the Gurson model is the consideration of a hardening flow stress σp. As it appears in both quadratic and exponential terms of the flow function, the calculation of σp is implicit. It impacts the numerical integration and it prevents the integration of the model into homogenized polycrystalline plasticity equations (the quadratic term is also problematic for the latter).

Conversely, the homogenization and limit analysis method of Rice and Gurson provides a unifying and powerful micromechanical framework for a large number of theoretical extensions (Benzerga and Leblond, 2010; Benzerga et al., 2016), which is not the case with the continuum thermodynamics derivation of the Rousselier model. Nevertheless, a heurisitic extension can be considered for this model, as proposed in Morgeneyer et al. (2009) for the GTN model: the mean macroscopic stress σ_m is substituted with σ_m^* to model 3D anisotropic void growth in an orthotropic material (principal axes of orthotropy: L, T, N). For isotropic void growth, $\alpha_L = \alpha_T = \alpha_N = 1/3$ and $\sigma_m^* = \sigma_m$:

$$\sigma_m^* = \alpha_L \sigma_{LL} + \alpha_T \sigma_{TT} + \alpha_N \sigma_{NN} \quad \text{with} \quad \alpha_L + \alpha_T + \alpha_N = 1. \tag{6}$$

Model	Gurson - GTN (1977-81-84)	Rousselier (1981)
Method of analysis	Micromechanics Limit load analysis	Thermodynamics Generalized normality rule
Geometrical basis	Hollow sphere, initial void volume fraction $f = f_0$	Any *isotropic* void distribution in a matrix, $f = f_0$
Boundary conditions	Axisymmetric	Not relevant (material point)
Theoretical material Plastic potential	Matrix: von Mises rigid-plastic, σ_{eq} = constant $2f$ **cosh**$(Q\sigma_m/\sigma^*)$, Q **= 3/2**	Matrix: hardening von Mises $\sigma_{eq}(\varepsilon^p{}_{eq}) = H(p)$, $p=\varepsilon^p{}_{eq}$ f **exp**(σ_m/σ_1), σ_1 = constant
Saturated hardening (real metallic alloy)	$\sigma^* = \sigma_{flow}$ = constant **Implicit** equation for $\sigma^*(\underline{\sigma},f)$	$\sigma_1 = \sigma_{flow}$ **/Q** = constant
Non saturated hardening (real metallic alloy)	*Heuristic* extension $\sigma^*(\underline{\sigma},f) = H(\varepsilon^p{}_{eq}) = H(p)$ **non constant**	p_1 *or* $\sigma_1 = H(p_1)$ /Q **constant** material parameter, *to be calibrated*
Strain rate and temperature effects	$\sigma^* = H(p, dp/dt, T)$	$\sigma_1 = H(p_1, dp/dt, T)$ /Q
Parameters (void growth measurements: $Q \cong 3/2$, $D = D_1 = 1.5 - 2$, for steels and aluminum alloys)	D **= 3/4 = 0.75**, *heuristic* extension (GT): q_1, q_2, q_3 $D = 3\, q_1 q_2 /4$ (*2***sinh**<exp) Most widely used: q_1 **= 1.5**, $q_2 = 1$, $q_3 = (q_1)^2 = 2.25$, D **= 9/8 = 1.125** << 1.5	$df/dp=(1-f)$ D_1 f **exp**(σ_m/σ_1) D_1 **= 3/2 = 1.5** from the ultimate state $f = f_u = 1$ at $\sigma_{eq}=\sigma_m=0$ Q **= 3/2** from the **NKCPML** (hereunder)
NKCPML: necessary kinematic condition of ***planar*** macroscopic localization (**2 D**): $\perp$ $d\varepsilon^p{}_m = d\varepsilon^p{}_{eq}$ **/2** *slant* $d\varepsilon^p{}_m < d\varepsilon^p{}_{eq}$ /2 NKCPML≈*coalescence*	**Not** fulfilled at large stress triaxiality Less and less fulfilled at increasing f values Only ***pointwise*** localization at $\sigma_{eq} = \sigma_m = 0$ (**0 D**) for $q_3 \le (q_1)^2$, $f = f_u \le 1/q_1$	*Normal* plane: fulfilled exactly at the vertex $\sigma_{eq} = 0$ for Q **= 3/2** More and more fulfilled at increasing f values *Slant* plane: fulfilled on the whole flow surface
Void damage in shear	Very small, null value in pure or simple shear $\sigma_m = 0$	Significant, pure shear included at large f values
Heuristic extension GTN ≈ *coalescence* for $f \ge f_C$ <<$f_u \Rightarrow (df/dt)*K$	Void growth acceleration function at *small* $f = f_C$ gives earlier *pointwise* localization	**No** f_C [an ultimate $0.2 \le f_u \le 0.3$ can be considered to define a *broken* state]
Regularization, characteristic length ℓ_c	Transforms the *pointwise* localization to volume (**3 D**) localization (*radius* ℓ_c)	Gives the *thickness* ℓ_c of the planar localization
Finite element discretization (size ℓ_c) Cartesian mesh →	Transforms the *pointwise* localization to volume (**3 D**) localization → and later to *planar* sheet of integration points (ℓ_c)	Transforms the *planar* localization to volume (**3 D**) localization → and later to planar sheet of integration points (ℓ_c)
Extension to multi-scale modeling	This quadratic and implicit model **cannot** be extended to polycrystalline plasticity	Polycrystalline plasticity Can be enhanced with additional models (plasticity, damage) at various scales

Figure 10. Comparison of the Gurson-Tvergaard-Needleman (1977-1981-1984) and Rousselier (1981) porous plasticity models. Constant *model* parameters to be calibrated are in red.

At the hydrostatic point, the Rousselier model does not verify the analytical solutions of the hollow cylinder or hollow sphere under pressure, contrary to Gurson-like models. It is not a fatal error, it reflects a fundamental difference between the two models: *void damage* (*without a defined geometric configuration of voids*) for the Rousselier model, *initial plasticity of a hollow sphere* for the original Gurson model. Consequently, between the two Cartesian axes, the slope of the flow surface varies in a much smaller interval than with the Gurson model: from $-D_1 f = -1/5$ to $Q = -3/2$ for the parameters of Fig. 3, vs. 0 to $-\infty$, with consequences for strain localization at all stress triaxialities and for damage in shear-dominated loadings.

The existence of a vertex on the σm axis has also been challenged, although in practice a pure hydrostatic tension is not encountered in numerical applications. Indeed, finite element limit load analyses of unit cells in axisymmetric loading also show a flat zone but this zone extends on both sides of the intersection of the yield locus with the σm axis in a (σ33 - σ11, σm) plane, showing no vertex (Benzergua and Leblond, 2010). But this result is limited to axisymmetric loadings for a *given* orientation of the localization plane that enables the use of σ33 - σ11 in place of σeq, it does not give the isotropic yield locus in function of σeq and σm. Besides, the representativeness of unit cell calculation vis-à-vis physical reality may also be questioned (Tekoğlu et al., 2015). It is not ascertained whether or not the Rousselier model is effective for these loadings $\sigma 11 = \sigma 22 > \sigma 33$.

With the GTN model, final failure is obtained for $f = f_F$ (also written $f = f_U$) much smaller than 1, which is consistent with experimental data. We recall that the "physical" f is kept distinct from the accelerated f^* used in the equations, which is unusual in modeling. With the Rousselier model, the final failure is for $f = 1$. Nevertheless, the stress-carrying capacity drops abruptly after the beginning of strain localization, as evidenced in Fig. 8 of the present paper (curves I and II) and in Fig. 7 of Rousselier et al. (1989), so failure is achieved for a much smaller void volume fraction, e.g. $f \approx 0.2$ in Fig. 7 of Rousselier et al. (1989). An ultimate value $f_u = 0.2$ or 0.3 can be introduced to define a "broken" state that shows the crack geometry and to avoid possible numerical problems, with a negligible impact on crack initiation and propagation (it is checked in the numerical applications of Section 4.2).

Void growth in the Rousselier model leads first to macroscopic strain localization in a plane and more or less later to the final failure. Tekoğlu et al. (2015) have calculated a doubly periodic array of voids within a normal or slant plane band confined between two outer blocks of the same material but without voids. These configurations are similar to the ones of Fig. 2. They obtained that macroscopic localization coincides with the onset of void coalescence for stress triaxiality $\eta < 1$. At triaxiality larger than 1, void coalescence requires additional plastic straining in the band. They conclude that the proper failure criterion to be used for failure analysis should be a macroscopic localization criterion based on void growth and not one based on void coalescence. They add that in some situations void coalescence must be modeled to account for all the energy dissipated in the failure process. It is in agreement with the standard use of the Rousselier model. Nevertheless, the work of Tekoğlu et al. (2015) questions the relation between strain localization and void coalescence. Additional calculations of the same configurations with porous plasticity models (GTN and Rousselier) would be valuable.

The parameter fc (supposed to be the onset of void coalescence in the GTN model) can also be discussed. In Koplik and Needleman (1988), the values of fc that matches well the unit cell calculations results (load and void volume fraction vs. macroscopic effective strain) appear to vary with stress triaxiality η (their calculations are for η = 1, 2 and 3), so it is not a constant material parameter. In Tekoğlu et al. (2015), the transition to uniaxial deformation corresponds approximately to $f = fc$ for $\eta = 1$ (it coincides with the onset of void coalescence) and the transition takes place for much smaller values $f << f$c for $\eta = 2$ and 3 (and void coalescence takes place for much larger values $f >> f$c). With the Rousselier model, the critical value of f is *predicted*, corresponding to the onset of strain localization, evidenced by the curves I and II of Fig. 8. In Fig. 8 of Rousselier (1981), it is also shown that this value is not a constant. In contrast, in the GTN model, fc is a *given* material parameter.

Constitutive equations cannot be validated without parameter identification, a key point in material modeling. An identification procedure of the two parameters σ1 and lc with notched tensile specimens has been proposed in Rousselier (1989, 2001a) and it is still valid. The parameters related to void characteristics: initial void volume fraction, shape, size distribution, nucleation model parameters, etc., are to be considered separately and calibrated with experimental observations at microscales, as much as possible. It can also be the case of lc,

although the relation between lc and interparticle spacing is not straightforward, and of D_1 if the recommended values 3/2 or 2 are too far apart from void growth measurements (rarely available). The heuristic extensions of the GTN model involve additional parameters (generally limited to three: $q1$, fc and K, Table 1, not to mention lc). There is no consensus on the choice of these parameters, as evidenced in the summary tables of Benseddiq and Imad (2008) and Yildiz and Yilmaz (2020) already quoted above.

The main conclusion is that both models are operational for finite element modeling of planar cracks initiation and propagation, but in somewhat different ways. This property is built-in in the Rousselier model. It results from the finite element discretization in the GTN model. For both models, discretization results in strain localization in finite volumes in the vicinity of integration points, generating a more or less flat layer with a finite thickness. Nevertheless, the response of the two models can be different, as mentioned in Besson et al. (2001): cup-cone fracture is more easily formed using the Rousselier model and it is related to the slope -3/2 at the vertex of the yield surface.

It is observed that the necessary kinematic condition of *planar* macroscopic localization is achieved in a small part of the GTN yield surface, excluding large stress triaxiality, and that with increasing void volume fraction, this small part shifts towards smaller stress triaxiality. At the opposite, with the Rousselier model the necessary kinematic condition of planar macroscopic localization is achieved in a large part of the yield surface, including large stress triaxiality, and with increasing void volume fraction, this part includes all positive stress triaxiality. In a certain way, Rice and Tracey's and Thomason's models for void growth and void coalescence, respectively, are merged into the Rousselier model.

The next section is devoted to multiscale modeling. It was mentioned in the introduction that the analytical form of Gurson's model makes it impossible to incorporate into self-consistent *polycrystalline* plasticity with a homogenized version of Eq. (2). It is also worth mentioning that extensions of the GTN-type yield surface using crystal plasticity have been developed via mean-field micromechanics schemes (e.g. Han et al., 2013; Ling et al., 2016). In these works, porous single crystals are considered. Eq. (2_1) is modified to apply at the slip system scale; it is an implicit equation for the resolved shear stress of each slip system. This model could be used within the so-called crystal plasticity finite element method (CPFEM) discussed at the beginning

of Section 4.1. It implies that the voids are small enough (i.e. submicrometric) to be considered as immersed in each crystal. In Section 4, Eq. (4) of the Rousselier model is homogenized in the case of a polycrystalline matrix and the micrometric voids are supposed to be large enough to be considered as immersed in the matrix material (submicrometric voids are modeled separately at the slip system scale).

4. Porous plasticity multiscale modeling.

4.1. Polycrystalline framework and ductile fracture.

Plasticity and ductile fracture are closely related because the latter results from the former. Therefore, a good modeling of ductile fracture first requires a good modeling of plasticity. Starting from Tresca and von Mises, macroscopic plasticity models have been dramatically improved (e.g. Hill, 1948; Hosford, 1985; Barlat and Lian, 1989; Bron and Besson, 2004; Kim et al., 2018; Lee et al., 2019). Another way of improvement is based on crystal plasticity modeling. The framework of physically based polycrystalline metal plasticity has intrinsic advantages in describing the anisotropy and distortion of the yield surface, as well as realistic anisotropic hardening. It enables the prediction of complex behaviors in multi-axial and multi-path loadings. (When damage and/or fracture are modeled, *local* loading paths are highly non-linear, even if the structure is in proportional loading.) Crystal plasticity is also used directly at the integration point scale in finite element modeling of polycrystalline aggregates, the so-called crystal plasticity finite element method (CPFEM). CPFEM has had a considerable development in recent years (e.g. Barbe et al., 2001a, 2001b; Gérard et al., 2013; Khadyko et al., 2016; Coudon et al., 2019; Farooq et al., 2020). But our objective is the numerical calculation of *macroscopic* laboratory specimens, which is not tractable with CPFEM. Polycrystalline plasticity requires strong modeling hypotheses that make it less “physical” than CPFEM, but the computation time can be limited to a few days, depending on the complexity of the model and on the size of the specimen mesh, provided a “reduced texture methodology” (RTM) is used to drastically limit the number of crystallographic orientations (Raabe and Roters, 2004; Rousselier et al., 2012). The Rousselier porous plasticity model can be embedded into the polycrystalline framework that also enables to introduce various plasticity and damage models at the slip system scale, e.g. a dynamic strain aging model (Rousselier and Quilici, 2015; Rousselier et al., 2017), the new

Coulomb ductile fracture model (Rousselier and Luo, 2014), nucleation and growth models of a second population of very small voids at the slip band scale (in the present paper).

In the classical polycrystalline framework, each of the N "grains" of the model represents a set of physical grains with close crystallographic orientations (also called "phase" in the literature). In the self-consistent models, each "grain" is considered as an inclusion in the homogeneous equivalent material: the "blue grain" in Fig 11a. Unlike in CPFEM, grain geometry, grain boundaries and intragranular heterogeneities are not captured in this framework. In the grains $g = 1$ to N, with volume fraction f_g and *homogeneous* stress tensor $\underline{\sigma}_g$ and plastic strain tensor $\underline{\varepsilon}_g^p$, $s=1$ to M slip systems are considered (e.g. for the FCC crystallographic structure, $M = 12$ octahedral slip systems {111}(100), for the BCC crystallographic structure, $M = 24$ slip systems).

A particular self-consistent polycrystalline model (Méric et al., 1991) was enhanced to model with accuracy the anisotropic plastic behavior at large strain (Rousselier et al., 2009, 2010; Luo and Rousselier, 2014). All equations are not recalled in the present paper, in particular the ones giving $\underline{\sigma}_g$ in function of an auxiliary strain tensor $\underline{\beta}_g$, the so-called "β model" (Cailletaud and Pilvin, 1994). The macroscopic plastic strain rate is the consequence of the slip rates $\dot{\gamma}_s$ of all the slip systems *s* in all grains *g*. The polycrystalline model was extended to porous plasticity in Rousselier and Leclercq (2006) and Rousselier and Luo (2014): the matrix material contains voids with a *variable* volume fraction f, as shown in Fig. 11b. The volume fractions of the matrix grains $g = 1$ to N are $(1-f)f_g$.

We can also consider a second population of very small voids that nucleate and grow in shear bands. These voids can contribute to void coalescence of the larger voids with the so-called "void sheet mechanism" (Fig. 11c). The transgranular crack can propagate in the neighboring grains. These geometrical features are not captured in the polycrystalline framework. In the model, a submicrometric void volume fraction f_s is attributed to the *M* slip systems of the grains $g = 1$ to N (like for $\dot{\gamma}_s$, the index g is omitted in the variable f_s to simplify some figures and equations, not to be mistaken with the *constant* volume fractions of the grains f_g).

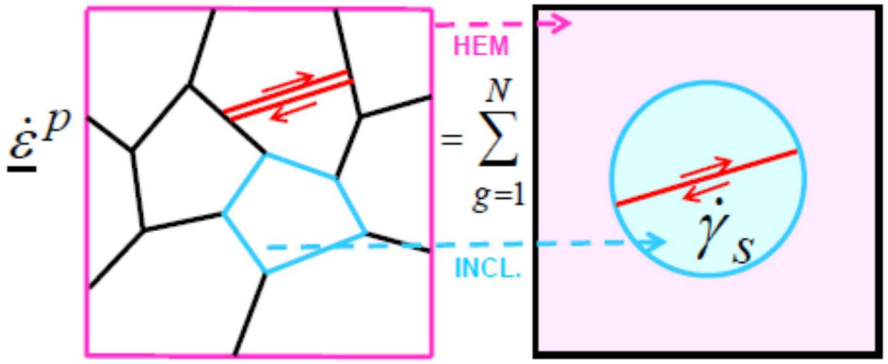

a)

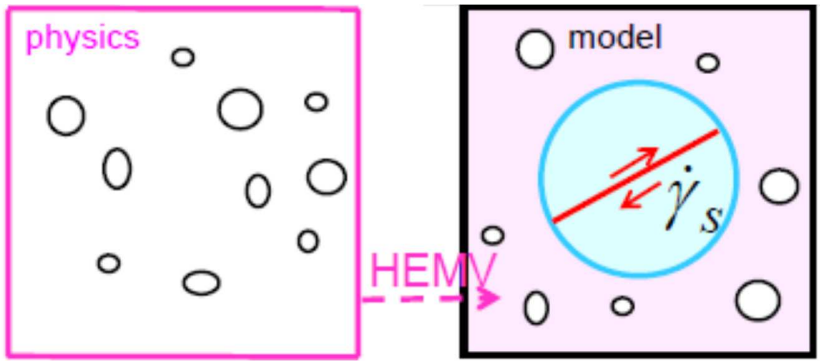

b)

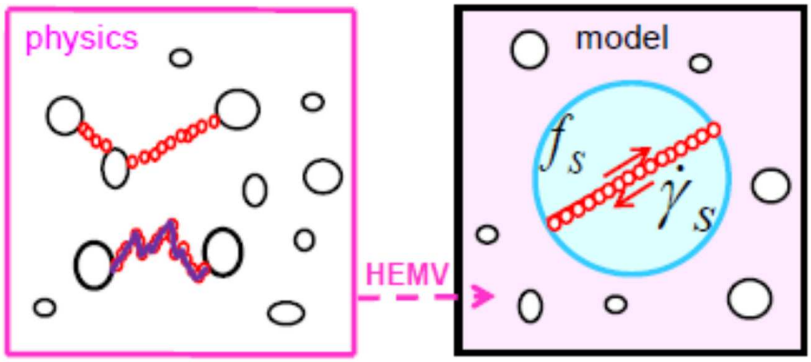

c)

Figure 11. a) Classical self-consistent polycrystalline framework. HEM: homogenized equivalent material, INCL.: inclusion. Physical mechanism on the left, model on the right. b) HEMV: homogenized equivalent material with voids. c) With submicrometric voids in shear bands, in particular between large voids (void sheet or zig-zag fracture).

The following plastic potential is used to derive the volumetric plastic strain rate:

$$F(\underline{\tau}) \cong F\left(\frac{\underline{\sigma}}{1-f}\right) = \frac{\sigma_{eq}}{1-f} - \left(\sum_{g=1}^{N} f_g \underline{\sigma}_g\right)_{eq} + D_1 \sigma_1 f \exp\left(\frac{\sigma_m^*}{(1-f)\sigma_1}\right) = 0 \qquad (7)$$

It has the same form as the macroscopic potential Eq. (4), except the second term which is the *matrix* flow stress, in place of the hardening curve $R(p)$ of the macroscopic model. For $D_1 = 0$, Eq. (7) corresponds to $\underline{\sigma} = (1-f)\sum f_g \underline{\sigma}_g$. For $f = 0$, it is the classical homogenization equation $\underline{\sigma} = \sum f_g \underline{\sigma}_g$. The resulting plastic strain rate is (the equivalent strain rate $\dot{\varepsilon}_{eq}^{p}$ is first calculated with the first deviatoric term only):

$$\underline{\dot{\varepsilon}}^{p} = (1-f)\sum_{g=1}^{N} f_g \sum_{s=1}^{M} \underline{m}_{sg} \dot{\gamma}_s + D_1 f \exp\left(\frac{\sigma_m^*}{(1-f)\sigma_1}\right) \dot{\varepsilon}_{eq}^{p} \underline{T}, \qquad \underline{T} = \begin{pmatrix} \alpha_L & 0 & 0 \\ 0 & \alpha_T & 0 \\ 0 & 0 & \alpha_N \end{pmatrix}$$

(8)

$\underline{m}_{sg}$ is the orientation tensor of each slip system. σ_m^* is defined in Eq. (6).

A phenomenological Norton-like viscoplastic model can be used for the constitutive equations of each slip system, depending on the resolved shear stress $\tau_s = \underline{\sigma}_g : \underline{m}_{sg}$:

$$\dot{\gamma}_s = \dot{v}_s \, Sign\,(\tau_s - X_s) \qquad (9)$$

$$\dot{v}_s = |\dot{\gamma}_s| = Max\left[0, \left(\frac{|\tau_s - X_s| - r_s}{K_s}\right)^{n_s}\right] \qquad (10)$$

$$r_s = r_s(v_s, v_t), \qquad \forall t \neq s \qquad (11)$$

$$\dot{\alpha}_s = \dot{\gamma}_s - d\alpha_s \dot{v}_s \quad , \quad X_s = c\alpha_s \qquad (12)$$

For each slip system, two scalar internal variables are introduced: $r_s = r_s(v_s, v_t)$ for isotropic hardening, depending on the cumulated slips $v_t = \gamma_t^{cum} = \int |\dot{\gamma}_t| dt$ of the $t = 1$ to M slip systems, and α_s for kinematic hardening. Equation (12) defines a nonlinear kinematic hardening model

with two parameters $_c$ and d . For large strain, experienced in particular in ductile fracture, it is necessary to combine at least two analytical curves in the isotropic hardening function r_s . Luo and Rousselier (2014) combined two saturated terms (Voce); it does not seem necessary to use a non-saturated function (Swift) to obtain a non-saturated flow stress:

$$r_s = R + \sum_{i=1}^{2} Q_i \sum_{t=1}^{M} H_i^{st} [1 - \exp(-b_i \gamma_t^{cum})] \tag{13}$$

The parameters (R, Q_1, b_1, Q_2, b_2) and (K, n) define work hardening and viscosity, respectively. In this paper, the initial critical resolved shear stress R is the same for all slip systems. The two *constant* hardening matrices H_1 and H_2 define the self-hardening of the slip systems (diagonal terms equal to 1) and the "latent" hardening (non diagonal terms) of all slip systems by already activated systems, which enables to model non proportional loadings. The use of two (*constant*) matrices makes it possible to model the evolution of latent hardening with large deformation, depending on the material parameters b_1 and b_2. (Another way to model large deformations would be to use a single *variable* hardening matrix.) Latent hardening has a key role in non-proportional loading. Moreover, texture evolution at very large deformation can be taken into account (Rousselier et al., 2009), but it is not as significant in ductile fracture as in metal forming and the computation time is multiplied by a factor in the order of 2; it is not used in this paper.

For the submicrometric voids, the contribution of all grains is added to the softening term of Eq. (7):

$$\frac{\sigma_{eq}}{1-f} - \left(\sum_{g=1}^{N} f_g \underline{\sigma}_g \right)_{eq} + \left(f + \sum_{g=1}^{N} f_g \left[\sum_{s=1}^{M} f_s \right]_g \right) D_1 \sigma_1 \exp\left(\frac{\sigma_m^*}{(1-f)\sigma_1} \right) = 0 \tag{14}$$

In Eq. (8), the volumetric strain rate is modified in the same way as in Eq. (14).

The void volume fraction rate is the sum of a first term for void growth and a second term for void nucleation:

$$\dot{f}_s = \left[(1 - f_s) D_{12} f_s \exp\left(\frac{|\tau_s|}{\tau_{12}} \right) + A_2 \right] \left(\frac{1}{2} \right) \dot{\gamma}_s \tag{15}$$

An exponential dependence on stress is chosen for the void growth term, similar to the one for the large voids. This equation is the most questionable one of the submicrometric voids model. Nevertheless, the relevant variables are present in this equation and it enables the first finite element calculations of laboratory specimens with secondary voids at the shear band scale. Voids in shear bands have been modeled in several papers, e.g. the nice parametric numerical analyses of Nielsen and Tvergaard (2011) who consider primary and secondary voids. But no simple analytical model is available. In the same framework, Eq. (15) can be changed when micromechanics studies deliver improved models. Moreover, void nucleation and void rotation are probably more significant than void growth for submicrometric voids modeling in shear bands.

The resolved shear stress τ_s can be positive or negative, but reverse loading is not specifically accounted for in nucleation models. Similar to D_1 and σ_1, D_{12} and τ_{12} are material parameters in which the subscript 2 is for the second population of voids. The ratio $1/2$ accounts for $\dot{\gamma}_s = 2\dot{\varepsilon}_s^p$ (slip rate = 2*shear strain rate) for the best oriented system in simple tension, corresponding to the largest values of τ_s and void damage; the plastic dissipation rate is $\tau_s \dot{\gamma}_s$ at the slip system scale vs. $\underline{\sigma} : \underline{\dot{\varepsilon}}^p$ at the macroscopic scale. For the same simple tension state, τ_{12} is expected to be close to $\sigma_1 / 2$. The parameter D_{12} can be chosen equal to D_1.

In Eq. (15), the factor A_2 is the same Gaussian function as in the void nucleation model of Chu and Needleman (1980). The cumulated equivalent plastic strain in the grain $[\underline{\varepsilon}_g]_{eq}^p$ substitutes the macroscopic one ε_{eq}^p, because the submicrometric voids mainly nucleate within the most deformed grains. Specific material parameters f_{N2}, σ_{N2} and ε_{N2} are used:

$$A_2([\underline{\varepsilon}_g]_{eq}^p) = \frac{f_{N2}}{\sigma_{N2}\sqrt{2\pi}} \exp\left[-\left(\frac{[\underline{\varepsilon}_g]_{eq}^p - \varepsilon_{N2}}{\sigma_{N2}\sqrt{2}}\right)^2\right] \tag{16}$$

Although this paper is devoted to porous plasticity, it cannot be overlooked that transgranular shear fracture without voids is observed in some metals, in particular in aluminum alloys (Chen, 2011; Luo et al., 2012; Buljac et al., 2018). A large amount of plastic deformation is necessary

prior to shear localization and fracture. In order to model this phenomenon, two distinct slip rates for each slip system are considered: the classical slip rate $\dot{\gamma}_S$ of Eq. (9) and an additional slip rate $\dot{\gamma}_s^C$ activated at large strains. The total slip rate is $\dot{\gamma}_s^{tot} = \dot{\gamma}_s + \dot{\gamma}_s^C$. In Eqs (8) and (15), $\dot{\gamma}_S$ is substituted with $\dot{\gamma}_s^{tot}$.

At the slip system scale, the only two stress components are the resolved shear stress τ_S and the normal stress σ_{nS}. The Coulomb (1773) brittle fracture model is a simple linear function of the two scalar variables. The new Coulomb ductile fracture model is a generalization at the microscopic scale of the Coulomb brittle fracture model at the macroscopic scale (Rousselier and Luo, 2014). For $|\tau_s| + c_0\sigma_{ns} \geq R_0$, the Coulomb slip γ_s^C and cumulated Coulomb slip $(\gamma_{cum}^C)_s = v_s^C$ are given by the viscoplastic rate equations:

$$\dot{v}_s^C = \dot{\gamma}_s^C \, Sign(\tau_s), \tag{17}$$

$$\dot{v}_s^C = Max\left[0, \left(\frac{|\tau_s| + c_0\sigma_{ns} - r_s^C}{K_0}\right)^{n_0}\right] \tag{18}$$

$$r_s^C = R_0 + Q_0[1 - \exp(-b_0 v_s^C)] \tag{19}$$

The novel feature (Rousselier and Luo, 2014) is a slow decrease (small parameter b_0) of the critical stress with γ_{cum}^C, resulting in progressive stress softening with a significant dissipation of mechanical energy and eventually in strain localization. Parameters Q_0 and b_0 can have arbitrary values (negative for Q_0). When b_0 goes to infinity, Coulomb's brittle fracture model without dissipation is recovered. It can be assumed that $Q_0 = -R_0$ for a total softening; in that case, the only "physical" parameters to be calibrated are c_0 and $R_0 >> R$. It can be assumed that $K_s = K_0$ and $n_s = n_0$ are the same for the plastic Eq. (10) and Coulomb Eq. (18) slip rates. The fracture model can be anisotropic because of the polycrystalline model framework (in

particular anisotropic hardening). It is non-associated (when $c_0 \neq 0$) because the normal stress σ_{ns} does not generate a normal strain rate.

4.2. Application to numerical simulation of laboratory specimens.

4.2.1. Ductile fracture of a thin Kahn specimen.

The material is 2198-T8R aluminum alloy. The 2.0 mm thick aluminum sheet was provided by Constellium in the recrystallized state and after an artificial ageing treatment (T8) generating submicrometric hardening precipitates. The composition is 2.9-3.5 Cu, 0.8-1.1 Li, 0.25-0.8 Mg, 0.1-0.5 Ag, 0.04-0.18 Zr (in wt.%), balance Al. The intermetallic particles volume fraction is ~0.3-0.4%, their size is 2-3 μm. Almost no initial porosity was found (<0.03 vol%). The grains are elongated to ~200-300 μm in the longitudinal L direction and to ~60 μm in the transverse T direction. The typical grain size in the short transverse S direction is ~25-30 μm. Three tensile tests were performed in the longitudinal, transverse and diagonal (45°) directions of the sheet plane (Chen, 2011; Chen et al., 2011). The yield strength is ~440 MPa and the ultimate tensile strength is ~500 MPa, showing relatively low work hardening. The material has moderate texture and tensile stress anisotropy measured in the sheet plane, but the Lankford ratios $L_k \approx 0.5$ are much smaller than 1, showing a significant mechanical anisotropy.

In Rousselier et al. (2017), dynamic strain aging (DSA) of this material was considered in the numerical simulations. It is not the case in the present work and the polycrystalline model parameters had to be calibrated again. An optimization software was used with the Levenberg-Marquardt algorithm (Levenberg, 1944). The reduced texture has three orthotropic texture components ($N = 12$). It is remarkable that the numerous plasticity parameters (including the reduced texture parameters) can be determined with three in-plane tensile tests only. The out-of-plane behavior is expected to be approximately predicted because all slip systems are activated with the in-plane tensile tests. Nevertheless, because no tension-compression test was available, the kinematic hardening parameters c and d of Eq. (12) are calibrated like a third isotropic hardening term at large strain (small exponent coefficient d). These two parameters are not representative of the real kinematic hardening of the material. Elasticity parameters are $E = 74{,}000$ MPa and $\nu = 0.3$. Viscosity parameters $n = 25$ et $K = 20$ MPa.s$^{1/n}$ are chosen to give a very small viscoplastic stress $K\dot{\gamma}^{1/n}$ for a large range of shear rates $\dot{\gamma}$.

The results are given in Figs 12 and 13. In Fig. 12a, the model red poles match with the concentrations of the experimental EBSD poles (stereographic projection). The dispersed EBSD poles are represented by the model purple and green poles. The "free of poles" zones are the same for the EBSD and model pole figures. There is no apparent contradiction between the model and real textures, although the former does not aim at representing exactly the latter, but only the resulting mechanical behavior. In Fig. 13, an excellent agreement is observed between the experimental and model tensile curves and thickness reduction curves.

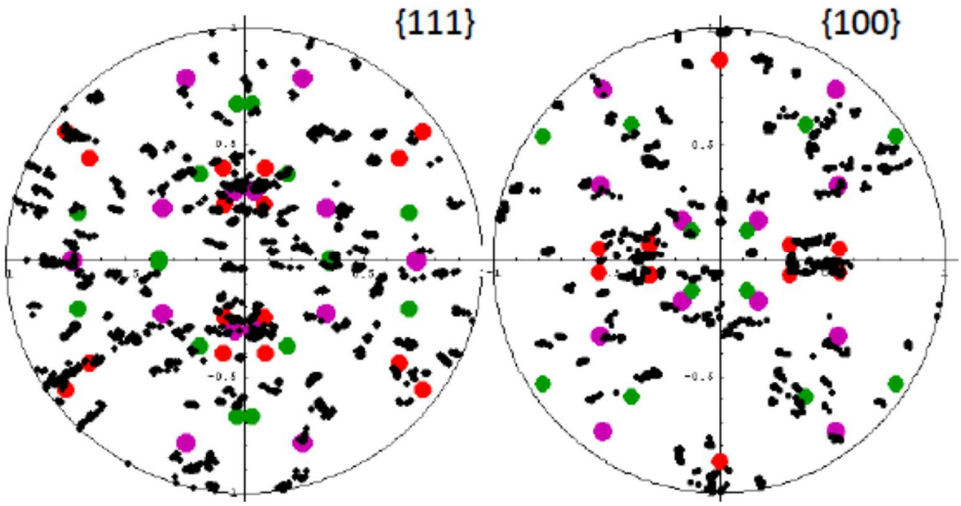

a)

phi1	PHI	phi2	frac	component
5.46669	56.20703	-10.01021	0.03942	0.158
46.60605	27.35035	-13.04489	0.12413	0.496
-133.1707	159.75935	-9.322238	0.08644	0.346

b)

r0	1.93919e+02	grd11	9.96993e+02	h1	1.74656e-01
Q	3.83373e+01	grd12	1.26356e+01	h2	1.96960e-01
b	7.88063e+00	grd13	3.69353e+02	h3	8.58757e-02
Q2	3.12626e+00	grd21	1.00000e+03	h4	5.00423e-02
b2	6.59966e-01	grd23	6.97351e+01	h5	8.62141e-02
c	3.31750e+01	grd31	1.39741e+02	k1	9.91430e-02
d	1.25516e+00	grd32	9.06676e+01	k2	1.23957e-01
		grd44	1.02142e+02	k3	9.32164e-02
C	20000	grd55	7.81913e+02	k4	1.35600e-01
		grd66	7.13619e+02	k5	1.56285e-01

Figure 12. a) Reduced texture of the 2198-T8R aluminum sheet, Euler angles, frac = volumic fraction of the $N = 12$ model crystallographic orientations, 3 orthotropic components with 4

orientations each. Small black discs: EBSD measurements. b) Polycrystalline model parameters. Hardening parameters of Eqs (12) and (13): r0 = R , Q = Q_1, Q_2 = Q_2 and c are in MPa. C (MPa) and grd are the anisotropic "β model" parameters (Sai et al., 2006), h and k are the hardening matrices parameters (non-diagonal terms), H = H_1 and K = H_2 (Luo and Rousselier, 2014).

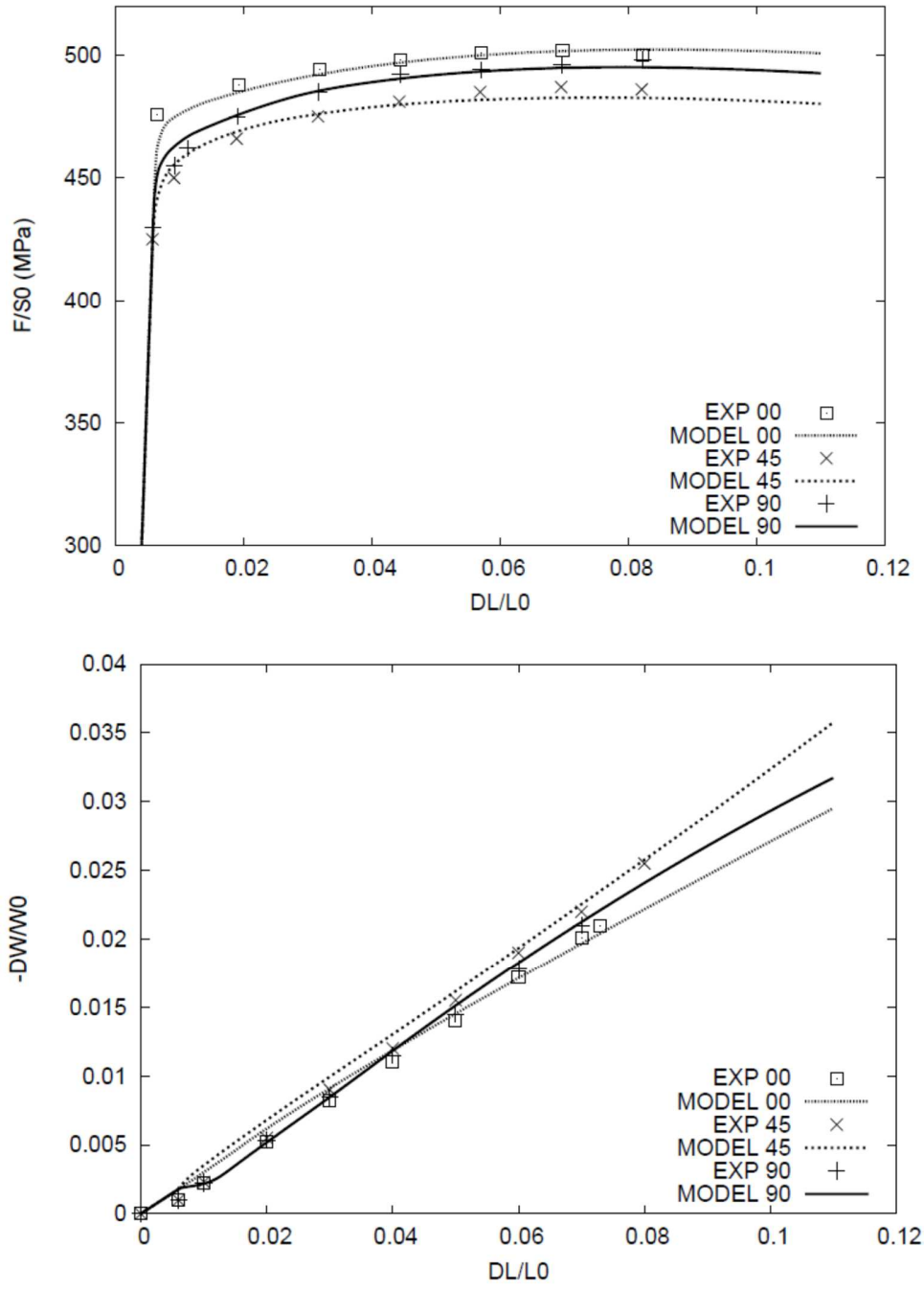

Figure 13. Engineering tensile curves and thickness reduction curves in the longitudinal (00), diagonal (45) and transverse (90) directions of the 2198-T8R aluminum sheet. Experimental points and calibrated model curves. The maximum elongation DL/L0 is applied in 100 s.

In Rousselier et al. (2017), a 1 mm-thick CT specimen of the same material was modeled, loaded at room temperature in the T-L direction. It was investigated with in situ X-ray laminography at the European Synchrotron Radiation Facility (Morgeneyer et al., 2014). Experimental data enabled to calibrate the ductile damage fracture parameters: porous plasticity and Coulomb ductile fracture models. But the experimental load was not measured. In this paper, we consider a KAHN specimen loaded in the T-L direction (Chen, 2011; Chen et al., 2011) and we investigate the effect of submicrometric voids on the load-displacement curve (crack initiation and propagation). The mesh is shown in Fig. 14, with a Cartesian mesh at the notch tip identical to the one of the CT specimen, in order to avoid mesh effects on ductile fracture.

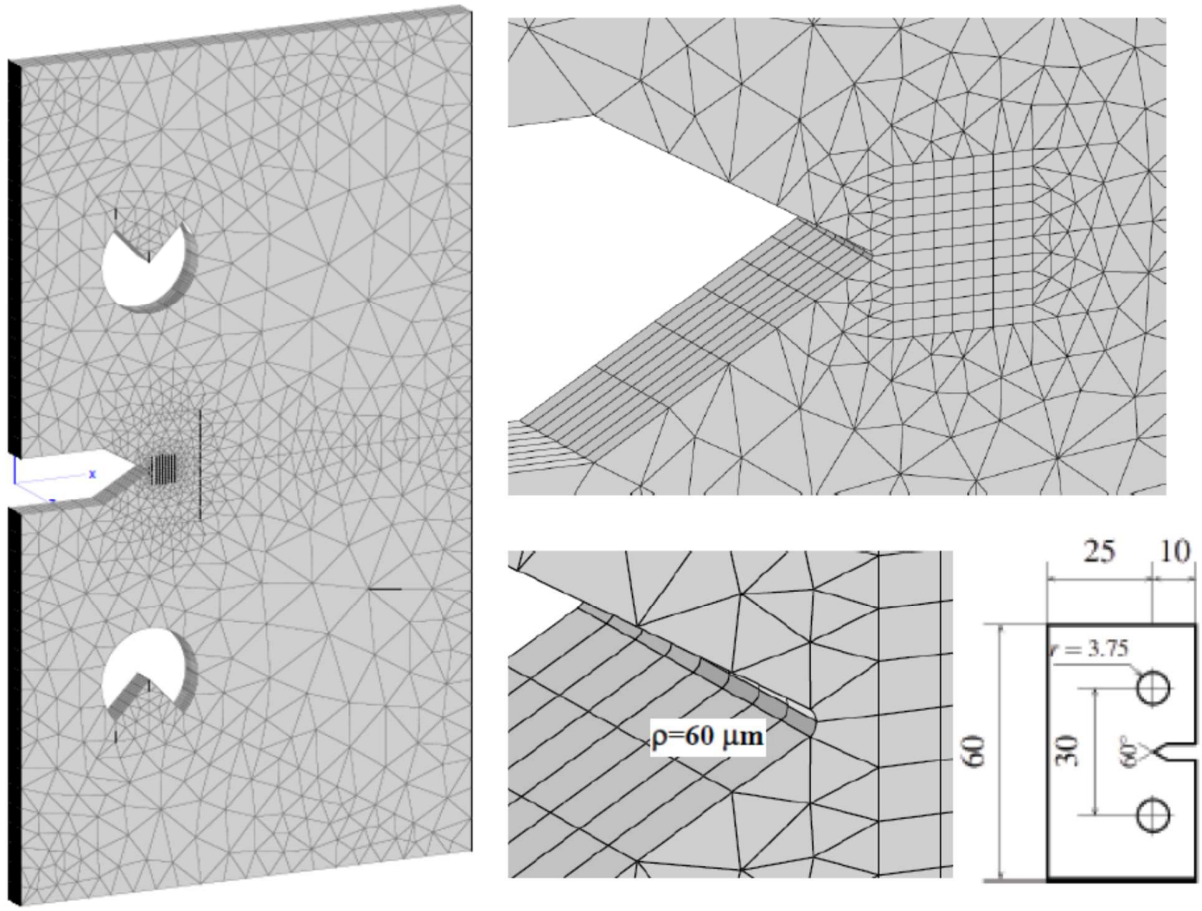

Figure 14. Finite element mesh of the KAHN specimen, thickness 2 mm. C3D15R and C3D20R reduced integration elements. Cartesian mesh at the notch tip (notch radius 60 µm), elements *initial* size: crack direction x=L 0.25 mm, loading direction y=T 0.20 mm, thickness 0.25 mm.

The fracture parameters are given in Table 1. They are the same as the ones used for the CT specimen, except $R_0 = -Q_0$ for the Coulomb model and the additional submicrometric voids parameters given later. The rather flat tensile curve enables to define a saturated stress σ_{flow} and the porous plasticity parameter $\sigma_1 = 2\sigma_{flow}/3 = 350$ MPa. The measured initial porosity and intermetallic particles volume fraction give f_0 for the micrometric voids and f_N (parameter of the Chu and Needleman void nucleation model). Because of the very small initial porosity volume fraction, the mean nucleation strain $\varepsilon_N = 0.1$ is the decisive parameter; this value is representative of the intermetallic particles and it matches well the experimental crack growth of

the CT specimen. Without experimental data for anisotropic void growth, $\alpha_L = \alpha_T = \alpha_N = 1/3$ is retained.

Table 1. Porous plasticity and Coulomb fracture model parameters.

D_1	σ_1[MPa]	f_0	f_N	ε_N	σ_N
2.	350.	0.0001	0.0034	0.1	0.02
c_0	R_0[MPa]	b_0	α_L	α_T	α_N
0.	285	2.	0.3333	0.3333	0.3333

In this paper, we only use the Coulomb model with $c_0 = 0$, because the computational cost is increased with a non associated model (the Coulomb model with $c_0 \neq 0$ is non associated) and mainly because the mechanical experiments do not enable to calibrate this parameter (in Rousselier and Luo (2014), the drastically different mechanical fields of the smooth notched tensile specimen and of the shear specimen made it possible to determine both parameters c0 = 0.05 and $R_0 = -Q_0$ = 105 MPa for a thin-walled 6260-T6 aluminum extrusion). $R_0 = -Q_0$ = 260 MPa used for the CT specimen was found to small to match the KAHN load-displacement curve (it was not possible to measure the load in the CT in-situ testing, and in the CT simulations the interaction of DSA and shear facture may also impact this parameter). For the KAHN specimen, $R_0 = -Q_0$ = 285 MPa gives an excellent agreement between the experimental red curve and the "NO secondary voids" curve D1 of Fig. 15.

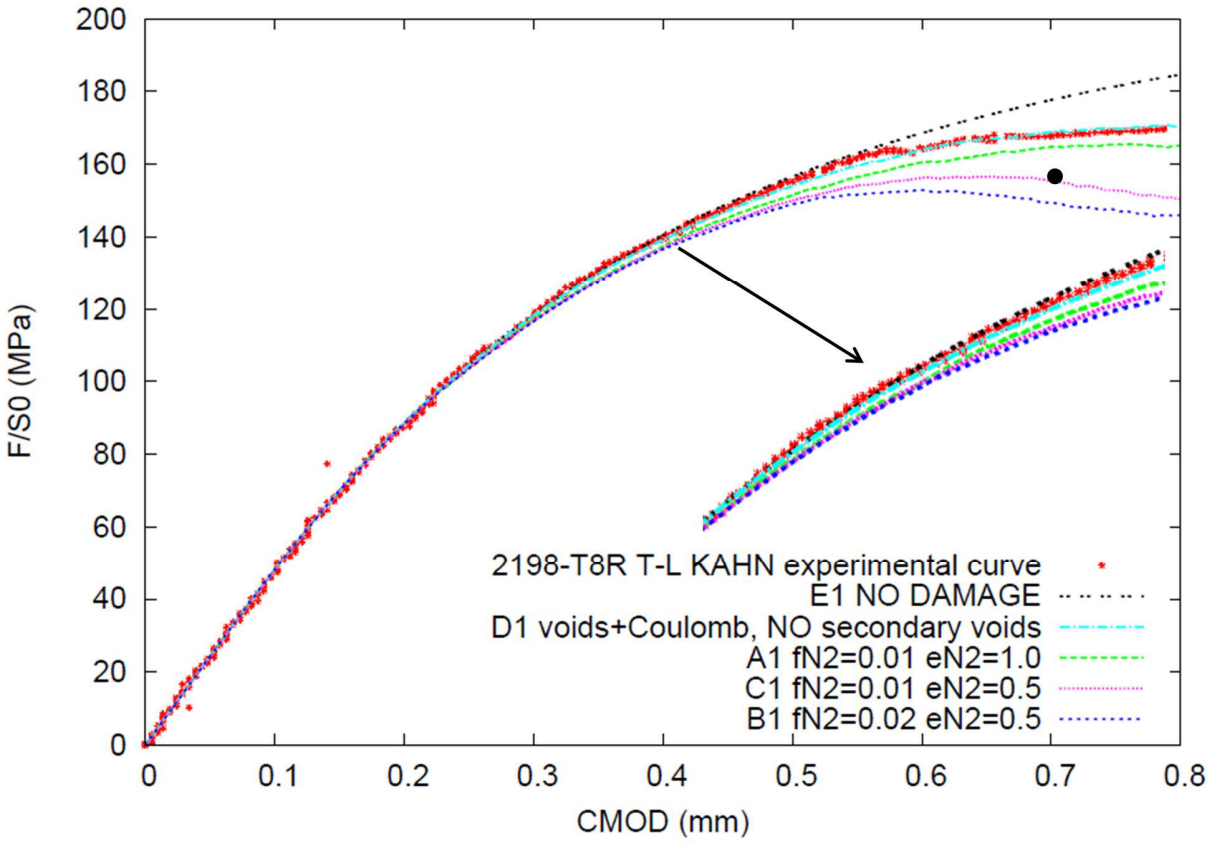

Figure 15. Load – CMOD curves of the 2198-T8R aluminum KAHN specimen. CMOD = crack mouth opening displacement, S0 = 25x2 = 50 mm^2. Small red points: experimental curve (cross head speed 0.1 mm/min). Numerical curves E-D-A-C-B correspond to increasing damage. Curves A-C-B are with submicrometric voids for various nucleation parameters.

The parameters of Eq. (33) are $D_{12} = D_1 = 2$ and $\tau_{12} = \sigma_1 / 2 = 175$ MPa. Fracture in Al-Cu-Li-based aluminum alloys has been reported to involve transgranular linkage in void sheets nucleated at matrix dispersoids (particle size in the range 10 nm-1 μm), which coalesce within shear bands (Tsivoulas and Prangnell, 2014). The dispersoids volume fraction is in the range 0.012-0.018% (Chen, 2011) and the nucleation strain is very large. In order to investigate the impact of dispersoids on ductile fracture, we have chosen two values 0.01 and 0.02 for the parameter f_{N2} of Eq. (34), and two values 0.5 and 1 for the parameter ε_{N2} (1 is probably closer to the real values), corresponding to the curves A1, C1 and B1 of Fig. 15. The standard deviation

σ_{N2} is 0.10 for curve A1 and 0.15 for curves C1 and B1. Provided Eqs (15) and (16) are an acceptable modeling, it can be concluded that dispersoids may have a significant effect on ductile fracture.

At the notch of the KAHN specimen, the *experimental* crack initiated at mid-thickness is flat in a small triangle approximately 1.5 mm large along the notch tip and 1.5 mm long in the notch plane (Chen, 2011). Two shear lips appear at the notch tip on the two free surfaces of the specimen, one in the upper part y>0 and one in the lower part y<0. The two shear lips join after approximately 1.5 mm crack propagation and form a slant crack. This experimental geometry is well modeled in the numerical simulation as evidenced by the "broken" integration points in Fig. 16, upper left. Fig. 16 corresponds to the black disc on curve C1 of Fig. 15. At this displacement (CMOD = 0.7045 mm, F/S0 = 155.11 MPa), the crack length is 2 mm. After this point, the mesh is no longer cartesian and the simulation is impacted by the mesh effect. For the flat crack, a *single layer* of broken points is obtained, located in the lower half of the specimen, i.e. the symmetric points in the upper half are not broken. The symmetry in the loading direction is lost for the flat crack, the shear lips and (of course) the slant crack. In the thickness direction, it is lost for the shear lips and the slant crack.

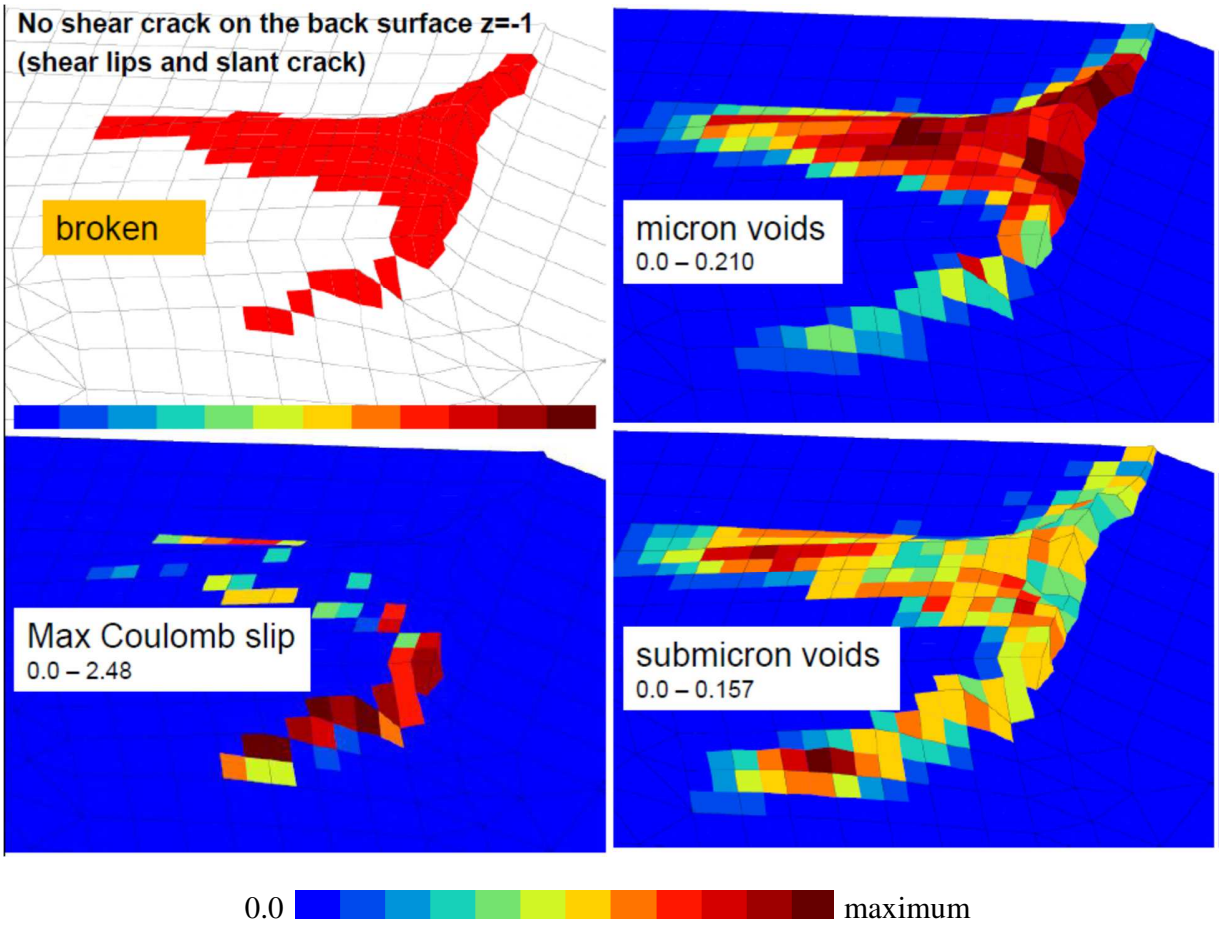

Figure 16. Damage variables at the KAHN specimen notch tip (located on the right of each figure), lower half of the specimen y≤0, deformed mesh. Clockwise from the upper left: 1) broken integration points showing the flat crack in the y = 0 plane and the shear lip on the front free surface z = 1 of the specimen, 2) void volume fraction f (maximum value in the specimen: 0.210, the colors correspond to the bar under the figure), 3) cumulated value of the submicrometric void volume fractions, Eq. (14) (maximum value in the specimen: 0.157), 4) largest value of $(\gamma^C_{cum})_s = v^C_s$ (maximum value in the specimen: 2.48).

Note that integration points are considered as "broken" when the non linear damage cumulative rule $(f_{tot}/f_u)^2 + (\max(\gamma^C_{cum})/\gamma^C_u)^2 = 1$ is obtained. In this equation, f_{tot} is the total volume fraction of Eq. (32). It enables to visualize the crack. The material behavior is then substituted with an elastic behavior with a very low stiffness (Young's modulus E = 1 MPa). The ultimate

values are $f_u = 0.25$ and $\gamma_u^C = 3$. We emphasize that these ultimate values are *not* material parameters to be calibrated, contrary to f_c in the GTN model. They just have to be large enough so that the load carrying capacity of the material is negligible. The simulation results depend little on these parameters: a second calculation of curve D1 of Fig 15 with $f_u = 0.15$ and $\gamma_u^C = 2$ gives F/S0 = 169.258 MPa at CMOD = 0.8 mm, compared to F/S0 = 170.270 in Fig. 15; the difference is 0.6%. In Fig. 11 of Rousselier and Luo (2014), it was shown that displacements at failure of flat notched tensile specimens also depend little (less than 1%) on these parameters in the same value ranges 0.15-0.25 and 2-3.

In Fig. 16, the contributions of the three damage models are compared. At mid-thickness and in the whole flat crack, stress triaxiality is larger and fracture is mainly due to micrometric void growth. In shear fracture, the contribution of submicrometric voids is significant but the Coulomb fracture model is predominant. It is in agreement with the nanometric dimples observed with MEB in the slant crack of the CT specimen (Morgeneyer et al., 2014) and with microtomography measurements on small pieces cut in KAHN specimens (Chen, 2011) that showed transgranular fracture in the slant crack without micrometric voids, see also Buljac et al. (2018). In the simulation, the submicrometric voids also contribute to the coalescence of the large voids in the flat crack (modeled by strain localization). These simulation results are also in agreement with what is obtained in similar materials (Tsivoulas and Prangnell, 2014). A more quantitative comparative analysis would need a comprehensive experimental study, for both parameter identification and validation of simulation results at various scales.

4.2.2. Effect of sulfur and carbon contents on ductile fracture of a low-alloyed steel.

In Tanguy (2001), ductile fracture mechanisms in notched tensile specimens were investigated. The material is A508 (16MND5) steel (0.16 C, 0.004 S, 1.33 Mn, 0.76 Ni, 0.22 Cr, 0.51 Mo, in wt %) which is used in the French pressurized water nuclear reactors. This material contains small round MnS inclusions at which micrometric voids are initiated at the very beginning of plastic deformation, so that it can be considered that f_0=1.75 10^{-4} is equal to the MnS volume fraction. At large deformation, nucleation of submicrometric voids was also observed with high magnification SEM at carbides of average size 0.1 μm (the approximate size range of all

carbides is 0.01-1 μm). The total volume fraction of carbides calculated from the chemical composition is $f_{N2} = 0.024$, but at fracture in the center of round notched tensile specimens the volume fraction of the carbides having initiated a void is only 0.006 (25%). The two other parameters of the nucleation statistical distribution were estimated: average initiation strain $\varepsilon_{N2} = 0.8$, standard deviation $\sigma_{N2} = 0.17$. Actually, ε_{N2} was obtained with the macroscopic strain of finite element simulations at the carbides locations in the specimen. It was observed that submicrometric voids only initiate in some grains (probably the most deformed ones), but the local deformations were not measured. As the model of Eq. (16) is based on the mean plastic strain of the grain, it is expected that the calibration of the nucleation model could be revisited.

The first task is to determine a reduced texture for this isotropic material. It takes several hundred random orientations to obtain a relatively isotropic behavior. In Rousselier at al. (2010), a texture reduced to only $N = 14$ orientations has been calibrated on a mechanical test basis computed with isotropic behavior: single and biaxial tension in many directions of a plane, various tests with shear, tension-shear orthogonal path. In this paper, with the tensile curve from Lorentz et al. (2008), the uniformity of the orientation density (Fig. 17a) on the 3D unitary hyper-sphere (in the 4D space) has been slightly improved with $N = 15$ orientations calibrated on the same test basis, which seems to be close to the optimum possible with this method: an attempt with $N = 18$ was not successful. The "isotropic" texture of Fig. 17a is symmetric with respect to the so-called RD and TD axes. It makes it possible to mesh only the 1/4 of a specimen which has the same symmetries, in particular the axisymmetric notched tensile specimens used in Tanguy (2001).

With this isotropic "universal" texture (actually slightly anisotropic), it only remains to calibrate the hardening parameters with the tensile curve of the steel (at room temperature). Because no tension-compression test was available, the kinematic hardening parameters c and d of Eq. (12) are calibrated like a third isotropic hardening term at large strain (small exponent coefficient d). The coefficients of the hardening matrices could not be identified: for the centered cubic crystallographic structure of steel, $M = 24$ and the structure of the 24x24 hardening matrices is not well known. It is assumed that the non-diagonal terms of each matrix all have the same value (one parameter per matrix). The value $h = k = 0.1$ was chosen for the two matrices. Elasticity parameters are $E = 198{,}000$ MPa and $\nu = 0.3$. Viscosity parameters $n = 25$ et $K = 20$ MPa.s$^{1/n}$ are

chosen to give a very small viscoplastic stress $K\dot{\gamma}^{1/n}$ for a large range of shear rates $\dot{\gamma}$ (the strain rate in the minimum section of the notched tensile specimens is in the order of 10^{-3} s^{-1}). With the calibrated parameters, the hardening curve is well modeled. The RD=TD and ND model curves are very close; it validates the reduced texture.

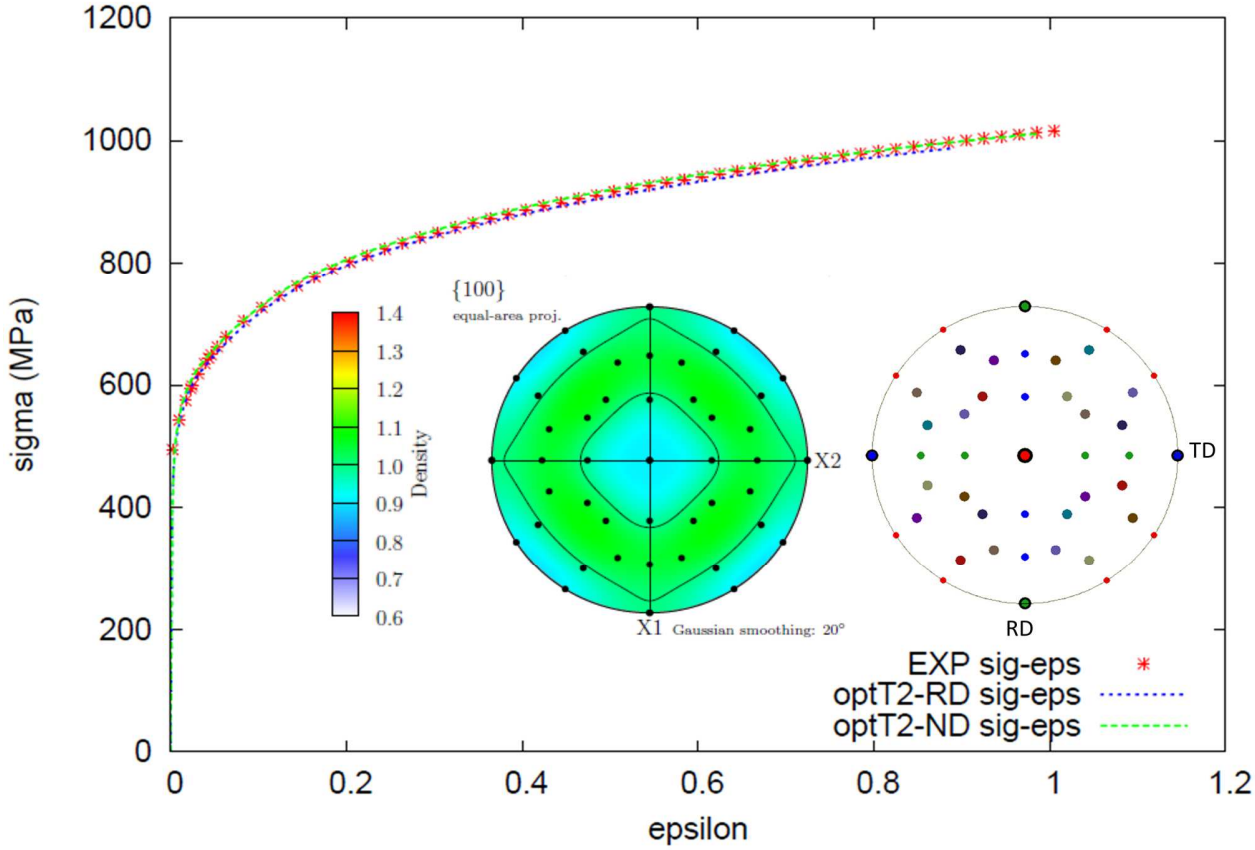

a)

b)

phi1	PHI	phi2	frac
0.	0.	0.	0.089826
32.343280	0.	0.	0.039175
-32.343280	0.	0.	0.039175
0.	32.34328	0.	0.039175
0.	-32.34328	0.	0.039175
90.	32.34328	-90.	0.039175
90.	-32.34328	-90.	0.039175
54.88219	-39.87235	-30.25177	0.084390
-54.88219	-39.87235	30.25177	0.084390
-54.88219	39.87235	30.25177	0.084390
54.88219	39.87235	-30.25177	0.084390
35.11781	-39.87235	-59.74823	0.084390
-35.11781	-39.87235	59.74823	0.084390
-35.11781	39.87235	59.74823	0.084390
35.11781	39.87235	-59.74823	0.084390

r0	182.754 MPa
Q	69.903 MPa
b	23.2538
Q2	49.725 MPa
b2	2.5988
c	66.811 MPa
d	0.53978
C	54321 MPa
grd_i=j	100.
grd_i≠j	0.
h	0.1
k	0.1

Figure 17. a) Isotropic reduced texture with N = 15 orientations, equal-area projection, orientation density (left) and {100} pole figure (right), the 3 poles of each orientation have the same color. True tensile curve representative of A508 steel at room temperature (red stars) and simulated curves in the x = RD (identical to z = TD) and y = ND directions (blue and green curves), with the reduced texture and the calibrated parameters. b) Euler angles and hardening parameters of Eqs (12) and (13). C and grd are the anisotropic "β model" parameters (Sai et al., 2006), h and k are the hardening matrices parameters (non-diagonal terms), H = H_1 and K = H_2.

Fig. 18a shows the mesh (1/4) of the central part of the round tensile specimen AE4 with a circular notch of radius 4 mm; the diameter of the minimum section is 10 mm. The load is applied in the vertical direction y = ND; the minimum section of the specimen is in the x-z = RD-TD plane of Fig. 17a. (Because of the slightly anisotropic reduced texture, the directions RD-TD-ND have to be specified.) The crack initiates in the center and propagates circularly over a *single layer* of integration points in the minimum section. The crack growth rate depends on the height of the elements, here 1/3 mm. Despite the symmetry, a 1/8 mesh (Fig. 18b) is not to be used, it would generate a crack on two layers of integration points and therefore a double dissipation.

a) 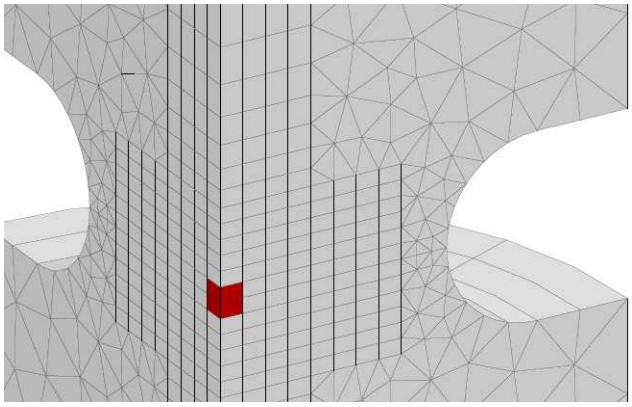 b) 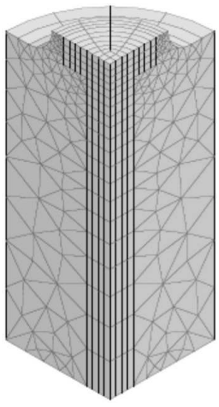

Figure 18. a) Mesh of the notch zone of AE4 round tensile specimen, center in red. C3D15R and C3D20R reduced integration elements. b) Half mesh y<0.

In order to investigate the combined effects of sulfur content (MnS inclusions) and carbon content (carbides), calculations were made for two values of the initial void volume fraction: f_0 = 0.0001 and 0.0015, corresponding to small and large values of the sulfur content, without and with submicrometric voids (4 calculations, Table 2). The Chu and Needleman nucleation model of Eq. (16) is used. With f_{N2} = 0.024, ε_{N2} = 0.8 and σ_{N2} = 0.1732, the calculated volume fraction of the carbides having initiated a void in the center of the specimen only is in the order of 10% of f_{N2}, much smaller than the measured value of 25%. In Tanguy (2001), the green model of Fig. 19 was used, based on a measured critical strain at nucleation around ε_c = 0.5. The corrected values f_{N2} = 0.024, ε_{N2} = 0.7 and σ_{N2} = 0.15 provide a much better agreement. These values are used in all the subsequent calculations. The other parameters are $D_1 = D_{12} = 2$, $\sigma_1 = 445$ MPa, the same values as for A508 steel in Rousselier et al. (1989), $\tau_{12} = \sigma_1 / 2$.

Table 2. AE4 specimen numerical simulations. Maximum load and diametral contraction ΔΦc at crack initiation (first broken integration point).

1	f_0= 0.0015	f_{N2} = 0.0	y = ND	$h = k$ = 0.1	69.62 kN	ΔΦc = 1.086 mm
2	f_0= 0.0015	f_{N2} = 0.024	y = ND	$h = k$ = 0.1	69.62 kN	ΔΦc = 1.068 mm
3	f_0= 0.0001	f_{N2} = 0.0	y = ND	$h = k$ = 0.1	70.52 kN	ΔΦc = 1.680 mm
4	**f_0= 0.0001**	**f_{N2} = 0.024**	y = ND	$h = k$ = 0.1	70.52 kN	**ΔΦc = 1.418 mm**
1.0	f_0= 0.0015	f_{N2} = 0.0	y = ND	**$h = k = 0$**	70.40 kN	**ΔΦc = 1.147 mm**
1.3	f_0= 0.0015	f_{N2} = 0.0	y = ND	$h = k$ = 0.3	69.79 kN	ΔΦc = 1.086 mm
1.010	f_0= 0.0015	f_{N2} = 0.0	y = TD	$h = k$ = 0.1	69.04 kN	ΔΦc = 1.077 mm
1.111	f_0= 0.0015	f_{N2} = 0.0	y ={111}	$h = k$ = 0.1	68.30 kN	ΔΦc = 1.064 mm

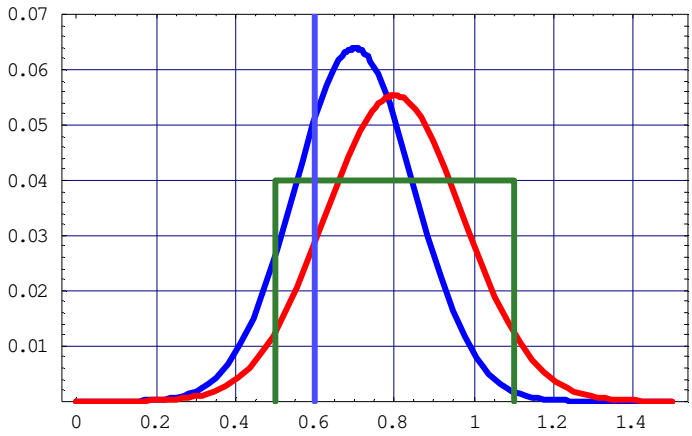

Figure 19. Statistical distributions of carbide nucleation with strain. Red (Gaussian) and green (constant with a critical strain ε_c = 0.5) for f_{N2} = 0.024, ε_{N2} = 0.8 and σ_{N2} = 0.1732. Blue: corrected Gaussian with f_{N2} = 0.024, ε_{N2} = 0.7 and σ_{N2} = 0.15; the vertical blue line at 0.5988 corresponds to 25% of the total volume fraction.

Fig. 20a shows the circular crack in the minimum section of the specimen (*single* layer of broken integration points, y<0) for f_0= 0.0015, *without* submicrometric voids. A point is broken when the ultimate value f_u = 0.2 is obtained. The layer of broken integration points is strongly stretched in the vertical loading direction, it corresponds to crack opening. In Fig. 20b, void growth is concentrated at the crack tip.

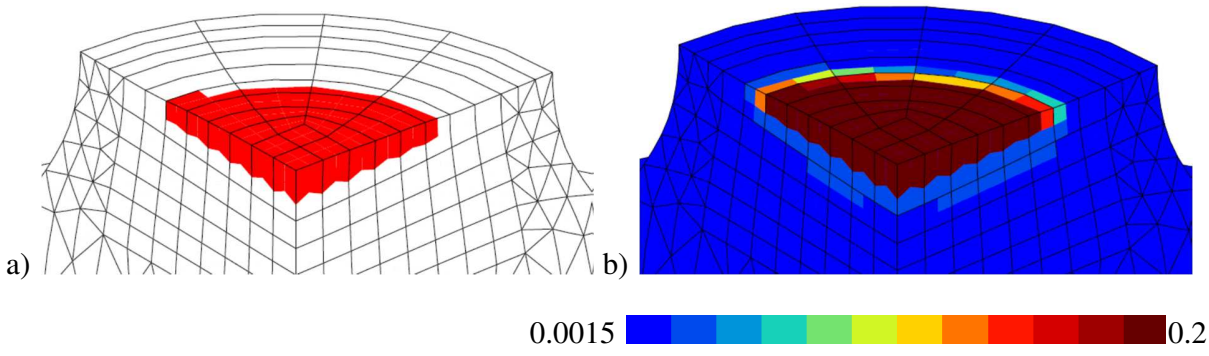

Figure 20. f_0= 0.0015, *without* submicrometric voids: a) broken integration points, b) void volume fraction.

The very large heterogeneity of plastic deformation is evidenced in Fig. 21a, b, c. At crack initiation in the specimen center, it ranges from 0.4 to 1.2 between the less and the most deformed grains, according to the crystallographic orientation. It highlights the leading role of nucleation depending on plastic strain in the grains and the requirement of multiscale modeling to simulate the effect of submicrometric voids in ductile fracture.

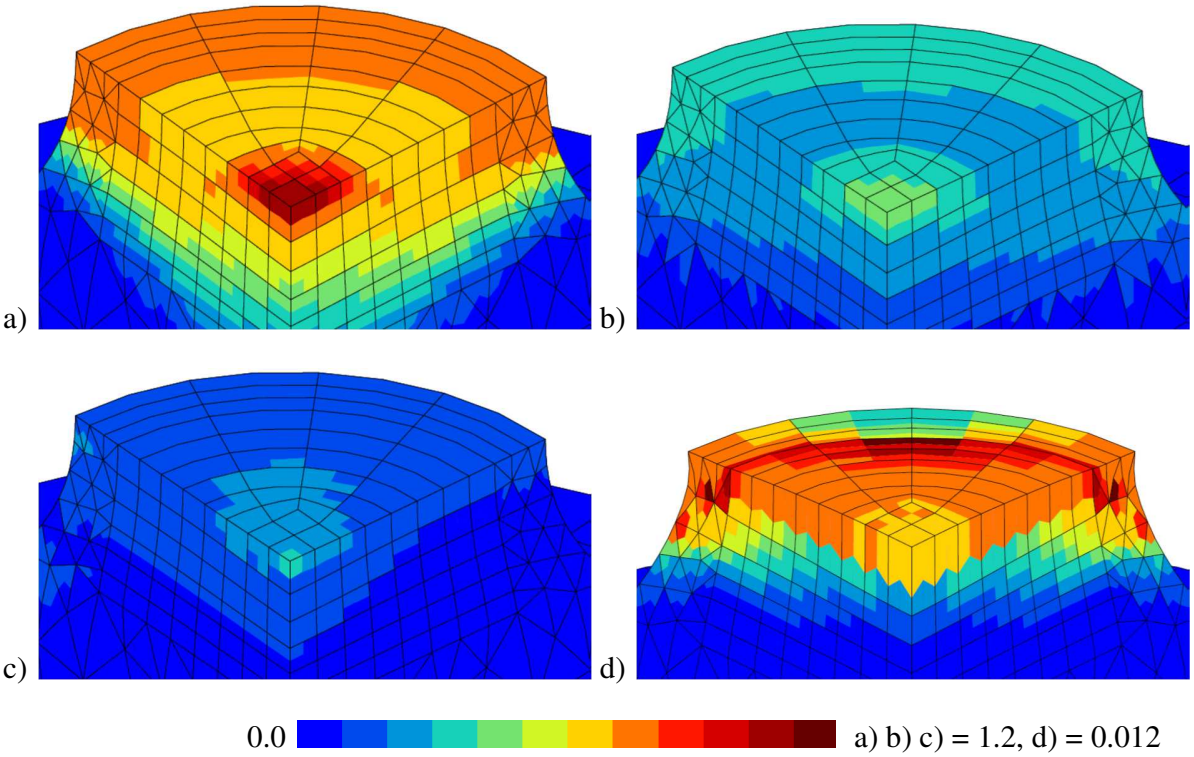

Figure 21. f_0= 0.0001, *with* submicrometric voids: a) b) c) clockwise from upper left, equivalent plastic strain heterogeneity, maximum-mean-minimum values at *crack initiation*. d) total volume fraction of carbides f_{carb} having initiated a submicrometric void at *complete failure* (0.006 in the specimen center, 0.012 in the notch, 25% and 50% of f_{N2} = 0.024, respectively).

Eq. (16) is integrated in each grain. The weighted sum per f_g gives the calculated total volume fraction of carbides f_{carb} having initiated a submicrometric void:

$$f_g^{carb} = \int \frac{f_{N2}}{\sigma_{N2}\sqrt{2\pi}} \exp\left[-\left(\frac{[\underline{\varepsilon}_g]_{eq}^p - \varepsilon_{N2}}{\sigma_{N2}\sqrt{2}}\right)^2\right] d[\underline{\varepsilon}_g]_{eq}^p \ , \quad f_{carb} = \sum f_g f_g^{carb} \qquad (20)$$

The integration stops when $f_{tot} = f_u$. In Fig. 21d, the values in the center of the specimen are close to 0.006, i.e. 25% of the volume fraction of all carbides, in agreement with the measured value in the same location. It validates the correction of the nucleation distribution (blue curve of Fig. 19), although in the real material f_0=1.75 10^{-4} is somewhat larger than in the simulation. It can also be observed that the nucleated fraction is larger in the part of the crack close to the notch (red zones in Fig. 21d) because the strains are larger there from the beginning of the loading (notch effect). In the notch area, it can be seen on the left and right sections of the specimen (x = 0 and z = 0 planes) that the nucleation model at large strain may *contribute* to the final shear failure (red zones corresponding to the cone of cup-cone fracture). The mesh design in the notch region with small triangles may facilitate shear failure, contrary to the mesh design of the KAHN specimen (Fig. 14) with triangles of increasing size at the right of the Cartesian mesh. At complete failure, the layer of broken integration points is strongly stretched in the vertical loading direction y, it corresponds to crack opening.

In Fig. 22, the elbows of the load-displacement curves correspond to crack initiation. Experimental curves are not shown because in this semi-parametric study the two values chosen for f_0 do not correspond to real materials but to minimum and maximum sulfur contents. It is known that notched tensile specimens are well modeled with porous plasticity, e.g. Rousselier et al. (1989) for A508 steel. In Tanguy (2001), f_0=1.75 10^{-4} and the experimental tensile curve is slightly different from the one used for the parameter calibration of Fig. 17, nevertheless the AE4 specimen experimental maximum load is 68.30 kN (corrected from the minimum section diameter 6 mm to 10 mm), very close to the values of Table 2. The experimental and numerical fracture behaviors cannot be compared because the parameter σ_1 and the element size in the loading direction (l_c = 1/3 mm) have not been calibrated. The final shear fracture in the notch area causes a sudden load drop (left red curve, f_0 = 0.0015).

When the sulfur content is large (left curves), the coalescence of the voids formed on the manganese sulfides occurs at small strains and only a small fraction of the carbides is nucleated

and contributes to strain localization. Therefore, submicrometric voids have little effect on the fracture resistance of the steel: the blue curve (with carbides) is close to the red curve (without carbides) for f_0 = 0.0015. The crack propagation rate (which determines the slope of the post-initiation curve) is a little larger with submicrometric voids than without. The effects of large contents of sulfur *and* carbon *do not cumulate* and the linear cumulative model used in safety rules seems much pessimistic. Conversely, at small sulfur content, the fracture strains are larger and the voids nucleated on carbides greatly reduce the ductility (right curves).

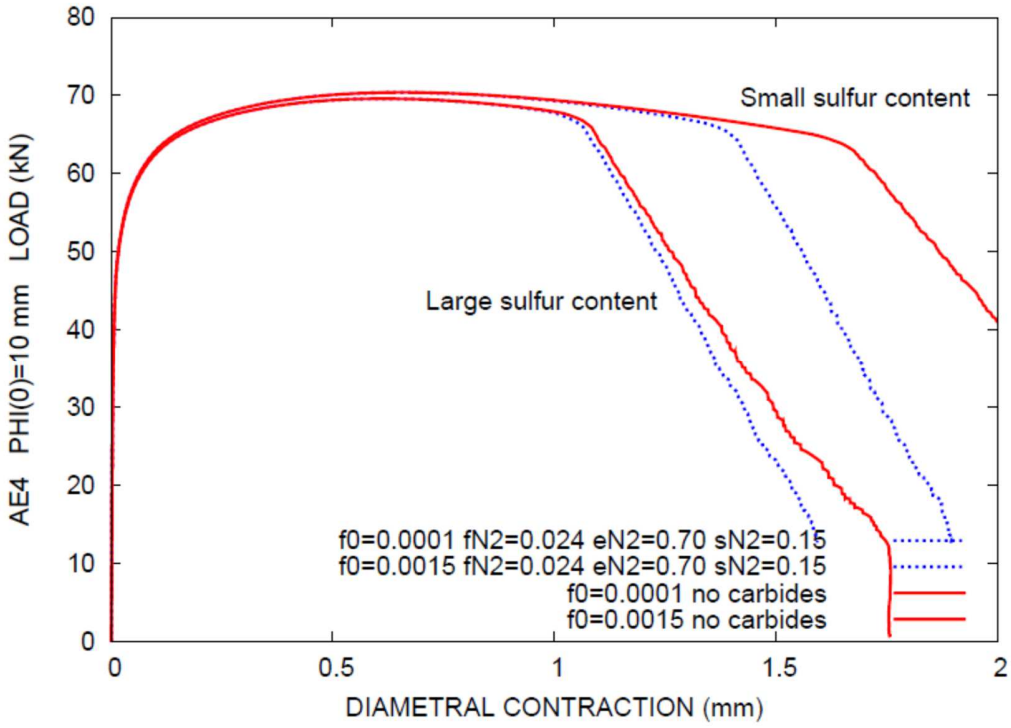

Figure 22. Load-displacement curves of the AE4 notched tensile specimen. Effect of sulfur and carbon contents in the MnNiMo low alloyed steel (voids nucleated on manganese sulfides and carbides, respectively).

In the notched tensile specimens, the loading paths at each point are not proportional because the plastic zone initiates in the notch and then propagates towards the axis. Damage in the center, crack initiation and propagation also induce non-proportional paths. The above calculations were performed with latent hardening parameters $h = k = 0.1$ for both hardening matrices. Two other calculations were performed with $h = k = 0.0$ and 0.3. The other hardening parameters have been

identified again in each case: an increase in h and k causes a sharp decrease in Q_1 and Q_2, R being little modified. The *overall* effect in plasticity is rather small since the load maximums are 70.40-69.62-69.79 kN for $h = k = 0.0$-0.1-0.3 (Table 2); the difference of 1% between 0.0 and 0.1 is nevertheless significant. Conversely, the deformation at crack initiation is markedly increased for $h = k = 0.0$ (blue interrupted curve in the insert of Fig. 23). It shows that macroscopic plasticity models, that have no latent hardening, introduce some bias in ductile fracture modeling. The absence of latent hardening is not realistic: a more complete study based on experimental tests and parameter calibration in plasticity and fracture would be necessary.

The deviation from isotropy (Fig. 17) is tested again in Fig. 23 for y = ND = {001}, y = TD = {010} and y = {111} loading directions. The 1/4 mesh is used for the {010} and {111} directions, although the symmetry of the reduced texture in the xz plane is then imperfect. The direction y = RD = {100} gives results identical to TD (symmetry of the reduced texture). The load maximums are 69.62-69.04-68.30 kN (Table 2), the scatter is less than ± 1%. This significant but acceptable value is the price to be paid for the polycrystalline plasticity simulation of an isotropic material at a reasonable numerical cost with a reduced texture. For an anisotropic material with a reduced texture, it is likely that the difference in results with the complete texture is of the same order of magnitude.

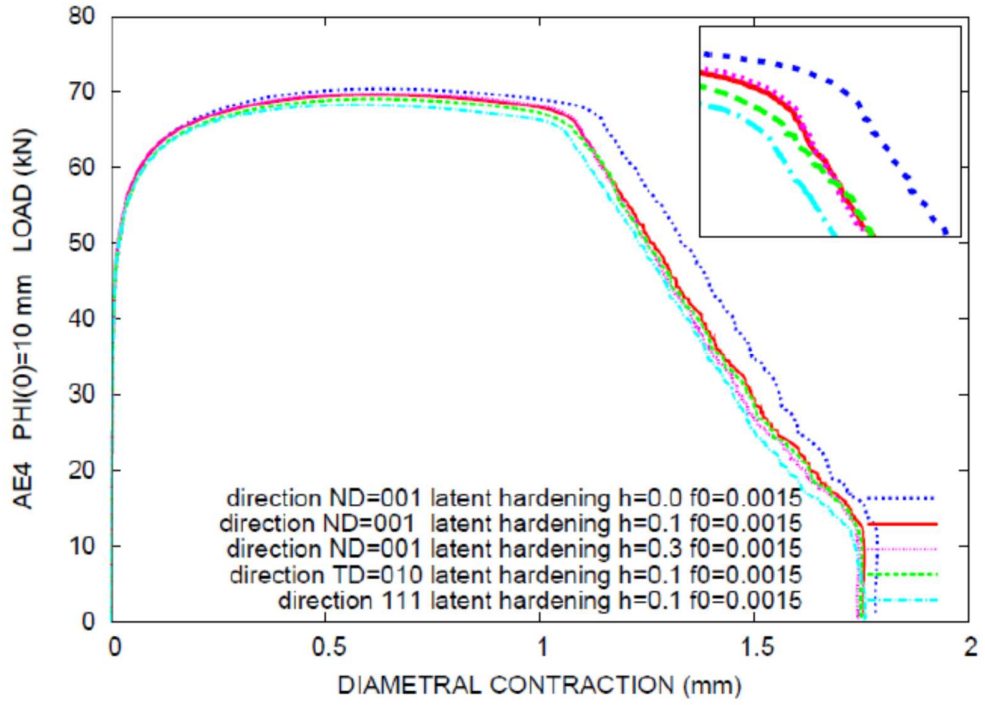

Figure 23. Load-displacement curves of the AE4 notched tensile specimen ($f_0 = 0.0015$). Latent hardening effect (ND tensile direction), tensile direction effect (for $h = k = 0.1$). All curves without secondary voids ($f_{N2} = 0$).

5. Conclusions.

The main objective of porous plasticity modeling is the finite element simulation of laboratory specimens. Forty years after the first finite element calculations (Rousselier, 1981; Tvergaard and Needleman, 1984), these models are not much used in structural calculations for automotive, aeronautic, pipeline, metal forming or nuclear industries. Reasons are parameter identification, computational cost and mesh dependence (related to strain localization). Regularization models that can solve the last issue are not considered in the present paper, partly because they increase the already large computational cost. Not one calculation but a large number is required in laboratory studies, e.g. the eight ones of Table 2 are only a very small part of the ones that were performed for this work. If we limit our goals to laboratory specimens, experimental-simulation and simulation-simulation comparisons are made with identical meshes. If a Cartesian mesh is embedded in the specimen mesh, the results should not be much impacted, including for shear fracture that may depend on the mesh orientation.

With this limited objective, the GTN and Rousselier models have been presented and discussed. Despite apparently similar, the analytical forms of these two models have fundamentally different mechanical consequences. The necessary kinematic condition of planar macroscopic localization (NKCPML) is more or less “built-in” in the Rousselier model but it is less and less fulfilled with the GTN model at increasing stress triaxiality and void volume fraction. We have shown that this issue is overcome by finite element discretization that transforms pointwise and planar localization into volume localization. It can now be understood why both models are operational for laboratory specimen calculations. These new results are illustrated by Figs 3 to 6 and by the local analysis of Fig. 9.

Because of its analytical form, only the Rousselier model can be integrated into the multiscale framework of self-consistent *polycrystalline* plasticity with a homogenized flow equation. Real textures are usually modeled by hundreds or more crystallographic orientations. Again the computational cost is prohibitive to perform numerous calculations. Not to mention CPFEM for

which *macroscopic* specimen calculations are not even an option, looking for example at the mesh of the KAHN specimen (Fig. 14), moreover limited to a very small crack growth (2 mm). A methodology that generates "reduced textures" (8 to 15 crystallographic orientations), calibrated with mechanical tests, brings a solution with a small loss of accuracy.

For macroscopic laboratory specimens calculations, the *polycrystalline* framework makes it possible to model at the slip system scale other mechanisms of plasticity: dynamic strain aging, and ductile fracture: transgranular crystallographic fracture, observed in particular in thin aluminum sheets, and for the first time in this framework the effect of a second population of submicrometric voids in aluminum alloys and in steels (nucleated on dispersoids and on carbides, respectively). These two latter applications are presented in the second part of the paper. Examples of specimen numerical simulations are given for these two classes of materials. For the submicrometric voids, the important effect of nucleation depending on plastic strain in the grains has been highlighted. The polycrystalline framework provides results that are not accessible with macroscopic models and that can be compared with experimental data (mechanisms, quantitative observations at various scales). In the applications to aluminum alloys and steel, only limited experimental data at the submicroscale were available. The contribution of synchrotron *nano*tomography (e.g. Nizery et al., 2015) could be decisive, for example with observations of small pieces cut in tested specimens, but at a high cost.

Acknowledgments

The author would like to thank Prof. Yazid Madi from MINES ParisTech for valuable discussions and for experimental data and Prof. Romain Quey from Ecole Nationale Supérieure des Mines de Saint-Etienne for valuable discussions and for the density equal-area projection of Fig. 17.

References

Barbe, F., Decker, L., Jeulin, D., Cailletaud, G., 2001a. Intergranular and intragranular behavior of polycrystalline aggregates. Part 1: F.E. model. Int. J. Plasticity 17, 513-536.

Barbe, F., Forest, S., Cailletaud, G., 2001b. Intergranular and intragranular behavior of polycrystalline aggregates. Part 2: Results. Int. J. Plasticity 17, 537-563.

Barlat, F., Lian, K., 1989. Plastic behavior and stretchability of sheet metals. Part I: A yield function for orthotropic sheets under plane stress conditions. Int. J. Plasticity 5, 51-66.

Benseddiq, N., Imad, A., 2008. A ductile fracture analysis using a local damage model, Int. J. Pressure Vessels and Piping 85, 219–227.

Benzerga, A. A., Besson, J., 2001. Plastic potentials for anisotropic porous solids. European Journal of Mechanics 20A, 397–434.

Benzerga, A., Leblond, J.-B., 2010. Ductile fracture by void growth to coalescence. Advances in Applied Mechanics 44, 196-305.

Benzerga, A., Leblond, J.-B., Needleman, A., Tvergaard, V., 2016. Ductile failure modeling. Itn. J. Frac. 201, 29-28.

Besson, J., Steglich, D., Brocks, W., 2001. Modeling of crack growth in round bars and plane strain specimens. Int. J. Solids Structures 38, 8259-8284.

Besson, J., Steglich, D., Brocks, W., 2003. Modeling of plane strain ductile rupture. Int. J. Plasticity 19, 1517-1541.

Besson, J., 2009. Damage of ductile materials under multiple plastic or viscoplastic mechanisms. Int. J. Plasticity 25, 2204-2221.

Bron, F., Besson, J., 2004. A yield function for anisotropic materials. Application to aluminum alloys. Int. J. Plasticity 20, 937-963.

Buljac, A., Hild, F., Helfen, L. Morgeneyer, T.F., 2018. On deformation and damage micromechanisms in strong work hardening 2198 T3 aluminum alloy, Acta Materialia 149, 29-45.

Chen, J.Q., 2011. Ductile tearing of AA2198 aluminum-lithium sheets for aeronautic applications. PhD thesis, Materials, Ecole Nationale Supérieure des Mines de Paris. <pastel-00657028>.

Chen, J.Q., Madi, Y., Morgeneyer, T.F., Besson, J., 2011. Plastic flow and ductile rupture of a 2198 Al-Cu-Li aluminum alloy**.** Comput. Mat. Sci. 50 (4), 1365-137.

Chen, Y., Lorentz, E., Besson, J., 2020. Crack initiation and propagation in small-scale yielding using a nonlocal GTN model**.** Int. J. Plasticity 130, 1-24, https://doi.org/10.1016/j.ijplas.2020.102701.

Chu, C.C., Needleman, A., 1980. Void nucleation effects in bi axially stretched sheets. J. Engng. Mater. Technol. – Trans. ASME 102, 249-256.

Coudon, F., Cailletaud, G., Cormier, J., Marcin, L., 2019. A multiscale model for nickel-based directionally solidified materials. Int. J. Plasticity 115, 1-17.

Coulomb, C.A., 1773. Sur une application des règles de maximis et minimis à quelques problèmes de statique, relatifs à l'architecture. In: Théorie des machines simples, 318-363.

Czanorta, C., Molinari, A., Mercier, S., 2020. Steady shock waves in porous metals: viscosity and micro-inertia effects. Int. J. Plasticity135, ***-***.

Enakoutsa, K., Leblond, J.-B., Perrin, G., 2007. Numerical implementation and assessment of a phenomenological nonlocal model of ductile rupture. Comput. Methods Appl. Mech. Engrg. 196, 1946-1957.

Farooq, H., Cailletaud, G., Forest, S., Ryckelynck, D., 2020. Crystal plasticity modeling of the cyclic behavior of polycrystalline aggregates under non-symmetric uniaxial loading: Global and local analyses. Int. J. Plasticity 126, 102619.

Fehringer, F., Seidenfuß, M., 2020. Experimental and numerical investigations on limit strains using an enhanced Rousselier model. Egnr. Fracture Mech., 226, https://doi.org/10.1016/j.engfracmech.2020.106868.

Feynman, R.P., 1963. Lectures on Physics, Volume 1: Mechanics, Section 45-3, p. 45-7. Addison-Wesley Publishing Company, Reading, Massachusetts.

Gérard, C., Cailletaud, G., Bacroix, B., 2013. Modeling of latent hardening produced by complex loading paths in FCC alloys. Int. J. Plasticity 42, 194-212.

Germain, P., Nguyen, Q.S., Suquet, P., 1983. Continuum thermodynamics. Trans ASME, J. Appl. Mech., 50(4b) (1983), 1010-1020, https://doi.org/10.1115/1.3167184.

Guo, J., Zhao, S., Murakami, R., Zang, S., 2013. Experimental and numerical investigation for ductile fracture of Al-alloy 5052 using modified Rousselier model. Computational Materials Science 71, 115-123.

Gurson, A.L., 1977. Continuum theory of ductile rupture by void nucleation and growth: part I—yield criteria and flow rules for porous ductile media. J. Engng. Mater. Technol. 99, 2-15.

Hadamard, J., 1903. Leçons sur la propagation des ondes et les équations de l'hydrodynamique, Paris, Chp. 6.

Han, X., Besson, J., Forest, S., Tanguy, B., Bugat, S., 2013. A yield function for single crystals containing voids. Int. J. of Solids and Structures 50, 2115-2131.

Hill, R., 1948. A theory of the yielding and plastic flow of anisotropic metals. Proc. Roy. Soc. London A193, 281-297.

Hosford, W.F., 1985. Comments on anisotropic yield criteria. Int. J. Mech. Sci. 27, 423–427.

Huang, Y., 1991. Accurate dilatation rates for spherical voids in triaxial stress fields, ASME Trans. J. Appl. Mech. 58, 1084-1085.

Kim, H., Barlat, F., Lee, Y., Zaman, S.B., Lee, C.S., Jeong, Y., 2018. A crystal plasticity model for describing the anisotropic hardening behavior of steel sheets during strain-path changes. Int. J. Plasticity 111, 85-106.

Khadyko, M., Dumoulin, S., Cailletaud, G., Hopperstad, O.S., 2016. Latent hardening and plastic anisotropy evolution in AA6060 aluminum alloy. Int. J. Plasticity 76, 51-74.

Koplik, J. Needleman, A., 1988. Void growth and coalescence in porous plastic solids, Int. J. Solids Structures 24, 835-853.

Landron, C., Maire, E., Bouaziz, O., Adrien, J., Lecarme, L., Bareggi, A., 2011. Validation of void growth models using X-ray microtomography characterization of damage in dual phase steels. Acta Mater. 59, 7564-7573.

Leclerc, J., Nguyen, V. D., Pardoen, T., Noels, L., 2020. A micromechanics-based non-local damage to crack transition framework for porous elastoplastic solids. Int. J. Plasticity 127, https://doi.org/10.1016/j.ijplas.2019.11.010.

Lee, E.H., Choi, H., Stoughton, T.B., Yoon, J.W., 2019. Combined anisotropic and distortion hardening to describe directional response with Bauschinger effect. Int. J. Plasticity 122, 73-88.

Levenberg, K., 1944. A method for the solution of certain non-linear problems in least squares. Quaterly of Applied Mathematics 2, 164-168.

Ling, C., Besson, J., Forest, S., Tanguy, B., Latourte, F., 2016. An elastoviscoplastic model for porous single crystals at finite strains and its assessment based on unit cell simulations. Int. J. Plasticity 84, 58-87.

Lorentz, E., Besson, J., Cano, V., 2008. Numerical simulation of ductile fracture with the Rousselier constitutive law. Comput. Methods Appl. Mech. Engng. 197, 1965-1982.

Luo, M., Dunand, M., Mohr, D., 2012. Experiments and modeling of anisotropic aluminum extrusions under multi-axial loading – part II: ductile fracture. Int.J. Plast. 32–33, 36–58.

Luo, M., Rousselier, G., 2014. Modeling of large strain multiaxial deformation of anisotropic metal sheets with strength-differential effect using a Reduced Texture Methodology, Int. J. of Plasticity 53, 66-89.

McClintock, F.A., 1968. A criterion of ductile fracture by the growth of holes. J. of Applied Mechanics 35, 363-371.

Maire, E., Zhou, S., Adrien, J., Dimichiel, M., 2011. Damage quantification in aluminum alloys using in situ tensile tests in X-ray tomography. Engrg. Fracture Mechanics. 78, 2679-2690.

Malcher, L., Andrade Pires, F.M., César de Sá, J.M.A., 2014. An extended GTN model for ductile fracture under high and low stress triaxiality. Int. J. Plasticity 54, 193-228.

Marini, B., Mudry, F., Pineau, A., 1985. Experimental study of cavity growth in ductile rupture. Engng. Fracture Mechanics 22, 989-996.

Méric, L., Poubanne, P., Cailletaud, G., 1991. Single crystal modeling for structural calculations - Part I: model presentation. J. Engng. Mater. Technol. 113, 162-170.

Monchiet, V., Cazacu, O., Charkaluk, E., Kondo, D., 2008. Macroscopic yield criteria for plastic anisotropic materials containing spheroidal voids. Int. J Plasticity 24, 1158–1189.

Morgeneyer, T.F., Besson, J., Proudhon, H., Starink, M.J., Sinclair, I., 2009. Experimental and numerical analysis of toughness anisotropy in AA2139 Al-alloy sheet. Acta Materialia 57, 3902-3915.

Morgeneyer, T.F., Taillandier-Thomas, T., Helfen, L., Baumbach, T., Sinclair, I., Roux, S., Hild, F., 2014. In situ 3-D observation of early strain localization during failure of thin Al alloy (2198) sheet. Acta Materialia 69, 78-91.

Nielsen, K.L., Tvergaard, V., 2011. Failure by void coalescence in metallic materials containing primary and secondary voids subject to intense shearing. Int. J. of Solids and Structures 48, 1255-1267.

Nizery, E., Proudhon, H., Buffiere, J.-Y., Cloetens, P., Morgeneyer, T.F., Forest, S., 2015. Three-dimensional characterization of fatigue-relevant intermetallic particles in high-strength aluminium alloys using synchrotron X-ray nanotomography, Philosophical Magazine 95:25, 2731-2746.

Raabe, D., Roters, F., 2004. Using texture components in crystal plasticity finite element simulations. Int. J Plasticity 20, 339–361.

Rice, J.R., Tracey, D.M., 1969. On the ductile enlargement of voids in triaxial stress fields. J. Mech. Phys. Solids 17, 201-217.

Rice, J.R., 1976. The Localization of Plastic Deformation. In: Koiter, W.T., (Ed.), Theoretical and Applied Mechanics, Proceedings of the 14th International Congress on Theoretical and Applied Mechanics, Delft, 1976, Vol. 1, North Holland Publishing Co., 207-220.

Rousselier, G., 1981. Finite deformation constitutive relations including ductile fracture damage. IUTAM symposium. In: Nemat-Nasser, S., (Ed.), Three-dimensional constitutive relations and ductile fracture. North-Holland, Amsterdam, 319-343, CNRS hal-02060680.

Rousselier, G., 1987. Ductile fracture models and their potential in local approach of fracture. Nuclear Engng. Design 105, 97-111.

Rousselier, G., J.-C. Devaux, G. Mottet, G. Devesa, 1989. A methodology for ductile fracture analysis based on damage mechanics: an illustration of a local approach to fracture. In Landes, J., Saxena, A., Merkle, J., (Eds), Nonlinear Fracture Mechanics: Volume II, Elastic-Plastic Fracture, STP995V2-EB, ASTM International, 1989, 332-354, https://doi.org/10.1520/STP27716S, CNRS hal-02081538.

Rousselier, G., 2001a. The Rousselier model for porous metal plasticity and ductile fracture. In: Lemaitre, J., (Ed.), Handbook of Materials Behavior Models. Academic Press, pp. 436-445.

Rousselier, G., 2001b. Dissipation in porous metal plasticity and ductile fracture. J. Mech. Phys. Solids 49, 1727-1746.

Rousselier, G., Leclercq, S., 2006. A simplified “polycrystalline” model for viscoplastic and damage finite element analyses. Int. J. Plasticity 22, 685-712.

Rousselier, G., Barlat, F., Yoon, J.W., 2009. A novel approach for anisotropic hardening modeling – Part I: Theory and its application to finite element analysis of deep drawing, Int. J. Plasticity 25, 2383-2409.

Rousselier, G., Barlat, F., Yoon, J.W., 2010. A novel approach for anisotropic hardening modeling – Part II: Anisotropic hardening in proportional and non-proportional loadings, application to initially isotropic material, Int. J. Plasticity 26, 1029-1049.

Rousselier, G., Luo, M., Mohr, D., 2012. Macroscopic plasticity modeling of anisotropic aluminum extrusions using a reduced texture methodology. Int. J.Plasticity 30-31, 144-165.

Rousselier, G., Luo, M., 2014. A fully coupled void damage and Mohr-Coulomb based ductile fracture model in the framework of a Reduced Texture Methodology, Int. J. Plasticity 55, 1-24.

Rousselier, G., Quilici, S., 2015. Combining porous plasticity with Coulomb and Portevin-Le Chatelier models for ductile fracture analyses. Int. J. Plasticity 69, 118-133

Rousselier, G., T.F. Morgeneyer, S. Ren, M. Mazière, S. Forest, 2017. Interaction of the Portevin-Le Chatelier phenomenon with ductile fracture of a thin aluminum specimen: experiments and simulations, Int. J. of Fracture 206, 95-122.

Sai, K., Cailletaud, G., Forest, S., 2006. Micro-mechanical modeling of the inelastic behavior of directionally solidified materials. Mech. Mater. 38, 203–217.

Sartori, C., Mercier, S., Jacques, N., Molinari, A., 2015. Constitutive behavior of porous ductile materials accounting for micro-inertia and void shape. Mech. Mater. 80, 324–339.

Seidenfuß, M., Roos, E., Samal, M.K., 2011. On critical assessment of the use of local and nonlocal damage models for prediction of ductile crack growth and crack path in various loading and boundary conditions. Int. J. Solids Structures 48, 3365-3381.

Tanguy, B. 2001.Modélisation de l'essai Charpy par l'approche locale de la rupture, application au cas de l'acier 16MND5 dans le domaine de transition, PhD thesis, Materials, Ecole Nationale Supérieure des Mines de Paris. <pastel-00005651>.

Tekoğlu, C., Hutchinson, J.W., Pardoen, T., 2015. On localization and void coalescence as a precursor to ductile fracture. Phil. Trans. R. Soc. A 373: 20140121.

Thomason, P.F., 1985. Three-dimensional models for the plastic limit-loads at incipient failure of the intervoid matrix in ductile porous solids, Acta Metall. 33, 1079-1085.

Tsivoulas, D., Prangnell, P.B., 2014. Comparison and effect of individual and combined Zr and Mn additions on the fracture behavior of Al-Cu-Li alloy AA2198 rolled sheet, Metall. and Mater. Trans. 45A, 1338-1351.

Tu, Y.H., Schmauder, S., Weber, U., Rudnik, Y., Ploshikhin, V., 2013. Simulation of the damage behavior of electron beam welded joints with the Rousselier model. Engrg. Fracture Mechanics 103, 153-161.

Tvergaard, V., 1981. Influence of voids on shear band instabilities under plane strain conditions. Int. J. of Fracture 17, 389-407

Tvergaard, V., Needleman, A., 1984. Analysis of cup-cone fracture in a round tensile bar. Acta Metall. 32, 157-169.

Vincent, P.-G., Suquet, P., Monerie, Y., Moulinec, H.,2014. Effective flow surface of porous materials with two populations of voids under internal pressure: I. A GTN model. Int J. Plasticity, 56, 45–73.

Weck, A., Wilkinson, D.S., Maire, E., Toda, H., 2008. Visualization by X-ray tomography of void growth and coalescence leading to fracture in model materials. Acta Mater. 56, 2919-2928.

Wilkerson, J.W., 2017. On the micromechanics of void dynamics at extreme rates. Int. J. Plasticity 95, 21–42.

Yildiz, R.A., Yilmaz, S., 2020. Experimental investigation of GTN model parameters of 6061 Al alloy. European J. of Mechanics A/Solids 83, https://doi.org/10.1016/euromechsol.2020.104040.

Figure captions

Figure 1. Ultimate value f^*_U in function of $q3$ for a given $q1$ (here $q1$=1.5, range $q3$ = 0 - 2.25).

Figure 2. Material element containing two plastically inactive blocks A and a band B of strain and damage localization. The material element is expanding in direction 1. a. without shear strain, b. with shear strain.

Figure 3. Gurson-GTN model yield locus in the (σ_m,σ_{eq}) plane for parameters: $f = 0.1$, Q = 3/2, σp = 1, $q_1 = 1.6245$, $q_2 = 1$, $q_3 = 2.25$. Rousselier porous plasticity model yield surface (blue curve) for parameters: $f_0 = 0$, $f = 0.1$, Q=3/2, $H = 1$, σ1 = H/Q =2H/3, $D_1 = 2$. NKCPML without and with shear strains, red arrows (slope -3/2) and blue arrows, respectively.

Figure 4. Gurson-GTN model, evolution of the yield locus in the (σ_m,σ_{eq}) plane with increasing void volume fraction for parameters: Q = 3/2, σp = 1, $q_1 = 1.6245$, $q_2 = 1$, $q_3 = 2.25$. The red line corresponds to a constant stress triaxiality equal to 2, the red discs correspond to the slope -3/2 (NKCPML)

Figure 5. Rousselier model, evolution of the yield locus in the (σ_m, σ_{eq}) plane with increasing void volume fraction for parameters $f_0 = 0$, $Q = 3/2$, $H = 1$, $\sigma 1 = H/Q = 2H/3$, $D_1 = 2$. *Insert:* zoom close to the axes origin.

Figure 6. Rousselier model, evolution of the yield locus. Same as Fig. 5 with $D_1 = 3/2$ in place of $D_1 = 2$. *Insert:* zoom close to the axes origin.

Figure 7. Pre-cracked three-point bent specimen (Rousselier, 1981), half mesh. Initial mesh (interrupted lines) and deformed meshes for two applied bending displacements showing strain localization in the initially thin elements. C (arrows) shows the crack tip.

Figure 8. Pre-cracked three-point bent specimen (Rousselier, 1981). Load-displacement curves for initial void volume fraction $f_0 = 10^{-2,}\ 10^{-3}$ and 10^{-4}. Stress component σ_{22} in the vertical direction for elements I and II at the crack tip. Note the functional expression of the damage variable β, with $\rho = (1-f)/(1-f_0)$.

Figure 9. Central part of the smooth tensile specimen axisymmetric mesh (Tvergaard and Needleman, 1984). *Left*: deformed mesh immediately after the sharp "knee" of the load vs. axial strain curve, corresponding to $f = f_c = 0.15$, $K = 5.2$. *Center:* Final deformed mesh. The blue disc is at the center of the specimen, the loading direction is horizontal. The red disc is the integration point closer to the center. *Right*: Initial geometry of the central quadrangle.

Figure 10. Comparison of the Gurson-Tvergaard-Needleman (1977-1981-1984) and Rousselier (1981) porous plasticity models. Constant *model* parameters to be calibrated are in red.

Figure 11. a) Classical self-consistent polycrystalline framework. HEM: homogenized equivalent material, INCL.: inclusion. Physical mechanism on the left, model on the right. b) HEMV: homogenized equivalent material with voids. c) With submicrometric voids in shear bands, in particular between large voids (void sheet or zig-zag fracture).

Figure 12. a) Reduced texture of the 2198-T8R aluminum sheet, Euler angles, frac = volumic fraction of the $N = 12$ model crystallographic orientations, 3 orthotropic components with 4 orientations each. Small black discs: EBSD measurements. b) Polycrystalline model parameters. Hardening parameters of Eqs (12) and (13): $r0 = R$, $Q = Q_1$, Q_2 and c are in MPa. C (MPa) and

grd are the anisotropic "β model" parameters (Sai et al., 2006), *h* and *k* are the hardening matrices parameters (non-diagonal terms), $H=H_1$ and $K=H_2$ (Luo and Rousselier, 2014).

Figure 13. Engineering tensile curves and thickness reduction curves in the longitudinal (00), diagonal (45) and transverse (90) directions of the 2198-T8R aluminum sheet. Experimental points and calibrated model curves. The maximum elongation DL/L0 is applied in 100 s.

Figure 14. Finite element mesh of the KAHN specimen, thickness 2 mm. C3D15R and C3D20R reduced integration elements. Cartesian mesh at the notch tip (notch radius 60 μm), elements *initial* size: crack direction x=L 0.25 mm, loading direction y=T 0.20 mm, thickness 0.25 mm.

Figure 15. Load – CMOD curves of the 2198-T8R aluminum KAHN specimen. CMOD = crack mouth opening displacement, S0 = 25x2 = 50 mm^2. Small red points: experimental curve (cross head speed 0.1 mm/min). Numerical curves E-D-A-C-B correspond to increasing damage. Curves A-C-B are with submicrometric voids for various nucleation parameters.

Figure 16. Damage variables at the KAHN specimen notch tip (located on the right of each figure), lower half of the specimen y≤0, deformed mesh. Clockwise from the upper left: 1) broken integration points showing the flat crack in the y = 0 plane and the shear lip on the front free surface z = 1 of the specimen, 2) void volume fraction *f* (maximum value in the specimen: 0.210, the colors correspond to the bar under the figure), 3) cumulated value of the submicrometric void volume fractions, Eq. (14) (maximum value in the specimen: 0.157), 4) largest value of $(\gamma_{cum}^{C})_s = v_s^C$ (maximum value in the specimen: 2.48).

Figure 17. a) Isotropic reduced texture with N = 15 orientations, equal-area projection, orientation density (left) and pole figure (right), the 3 poles of each orientation have the same color. True tensile curve representative of A508 steel at room temperature (red stars) and simulated curves in the x = RD (identical to z = TD) and y = ND directions (blue and green curves), with the reduced texture and calibrated parameters. b) Euler angles and hardening parameters of Eqs (12) and (13). C and grd are the anisotropic "β model" parameters (Sai et al., 2006), *h* and *k* are the hardening matrices $H=H_1$ and $K=H_2$ non diagonal parameters.

Figure 18. a) Mesh of the notch zone of AE4 round tensile specimen, center in red. C3D15R and C3D20R reduced integration elements. b) Half mesh y<0.

Figure 19. Statistical distributions of carbide nucleation with strain. Red (Gaussian) and green (constant with a critical strain ε_c = 0.5) for f_{N2} = 0.024, ε_{N2} = 0.8 and σ_{N2} = 0.1732. Blue: corrected Gaussian with f_{N2} = 0.024, ε_{N2} = 0.7 and σ_{N2} = 0.15; the vertical blue line at 0.5988 corresponds to 25% of the total volume fraction.

Figure 20. f_0= 0.0015, *without* submicrometric voids: a) broken integration points, b) void volume fraction.

Figure 21. f_0= 0.0001, *with* submicrometric voids: a) b) c) clockwise from upper left, equivalent plastic strain heterogeneity, maximum-mean-minimum values at *crack initiation*. d) total volume fraction of carbides having initiated a submicrometric void at *complete failure* (0.006 in the specimen center, 0.012 in the notch, 25% and 50% of f_{N2} = 0.024, respectively).

Figure 22. Load-displacement curves of the AE4 notched tensile specimen. Effect of sulfur and carbon contents in the MnNiMo low alloyed steel (voids nucleated on manganese sulfides and carbides, respectively).

Figure 23. Load-displacement curves of the AE4 notched tensile specimen (f_0 = 0.0015). Latent hardening effect (ND tensile direction), tensile direction effect (for $h = k = 0.1$). All curves without secondary voids (f_{N2} = 0).

Table headings

Table 1. Porous plasticity and Coulomb fracture model parameters.

Table 2. AE4 specimen numerical simulations. Maximum load and diametral contraction ΔΦc at crack initiation (first broken integration point).